AD-A162 300 STUDY IN SPURIOUS SENSITIVITY OF ELECTRONICS IN SPACE 1/1
(U) ITT AEROSPAEE/OPTICAL DIV FORT WAYNE IND
D M YEAGER 01 AUG 85 AFOSR-TR-85-0983 F49620-83-C-0153

UNCLASSIFIED F/G 9/1 NL

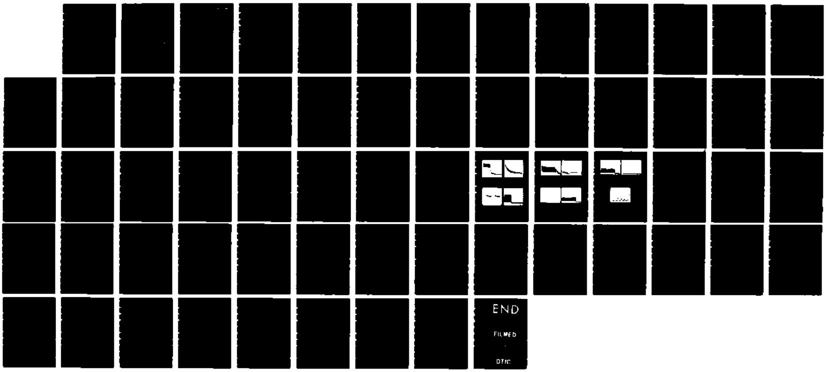

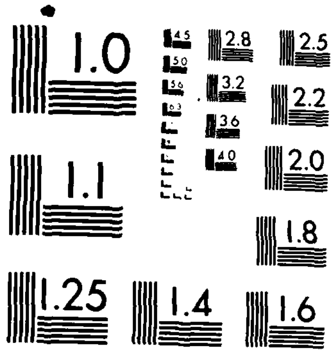

MICROCOPY RESOLUTION TEST CHART
NATIONAL BUREAU OF STANDARDS-1963-A

AFOSR-TR- 85-0983

(2)

STUDY IN SPURIOUS SENSITIVITY OF ELECTRONICS IN SPACE

BY

DAVID M. YEAGER

AD-A162 300

PREPARED BY:

ITT - AEROSPACE/OPTICAL DIVISION
P.O. BOX 3700
FORT WAYNE, INDIANA 46801

AUGUST 1, 1985

FINAL REPORT

CONTRACT NO. F49620-83-C-0153

PREPARED FOR:

AIR FORCE OFFICE OF SCIENTIFIC RESEARCH
BUILDING 410
BOLLING AFB, DC 20332

UNCLASSIFIED

SECURITY CLASSIFICATION OF THIS PAGE

AD-A[illegible]

REPORT DOCUMENTATION PAGE

1a. REPORT SECURITY CLASSIFICATION: UNCLASSIFIED

1b. RESTRICTIVE MARKINGS:

2a. SECURITY CLASSIFICATION AUTHORITY:

2b. DECLASSIFICATION/DOWNGRADING SCHEDULE:

3. DISTRIBUTION/AVAILABILITY OF REPORT: Approved for public release; distribution unlimited.

4. PERFORMING ORGANIZATION REPORT NUMBER(S):

5. MONITORING ORGANIZATION REPORT NUMBER(S): AFOSR-TR- 85-0983

6a. NAME OF PERFORMING ORGANIZATION: ITT Aerospace/Optical Division

6b. OFFICE SYMBOL *(If applicable)*:

7a. NAME OF MONITORING ORGANIZATION: Air Force Office of Scientific Research

6c. ADDRESS *(City, State and ZIP Code)*: P.O. Box 3700, Fort Wayne, Indiana 46801

7b. ADDRESS *(City, State and ZIP Code)*: Building 410, Bolling AFB, DC 20332

8a. NAME OF FUNDING/SPONSORING ORGANIZATION: AFOSR/NE

8b. OFFICE SYMBOL *(If applicable)*: NE

9. PROCUREMENT INSTRUMENT IDENTIFICATION NUMBER: F49620-83-C-0153

8c. ADDRESS *(City, State and ZIP Code)*: Same as 7b

10. SOURCE OF FUNDING NOS.

PROGRAM ELEMENT NO.	PROJECT NO.	TASK NO.	WORK UNIT NO.
61102F	2301/A7		

11. TITLE *(Include Security Classification)*: Study in Spurious Sensitivity of Electronics in Space-Final Report

12. PERSONAL AUTHOR(S): David M. Yeager

13a. TYPE OF REPORT: Final

13b. TIME COVERED: FROM 1/84 TO 8/84

14. DATE OF REPORT *(Yr., Mo., Day)*: 1 August 1985

15. PAGE COUNT: 55

16. SUPPLEMENTARY NOTATION:

17. COSATI CODES

FIELD	GROUP	SUB. GR.

18. SUBJECT TERMS *(Continue on reverse if necessary and identify by block number)*: Photodiode Sensors, 132 MeV protons, Radiation Sensitivity Protons, Multiplier Phototubes, Silicon Photodiodes,

19. ABSTRACT *(Continue on reverse if necessary and identify by block number)*

The results of an experimental investigation into the interaction of protons, E = 318 MeV and 132 MeV, with selected multiplier phototubes and silicon photodiodes are presented. The devices were chosen because of their spaceborne applications and previous gamma ray, electron, and lower energy proton measurements. The energies are representative of those expected of particle beam weapons.

A discussion of the operation of each device and its expected response to protons is presented. Testing at Los Alamos Meson Physics Facility demonstrated the temporal response of multiplier phototubes to be nanoseconds but requires microseconds for decay. Another test at the Harvard Cyclotron Laboratory determined the transient response of these sensors to 132 MeV protons in the range of 10^5 to 2×10^8 P/cm^2 sec. The response was very nearly linear, but was slightly less for most devices. The radiation sensitivity of each device was calculated as expected. The multiplier phototubes were the least sensitive.

(continued)

20. DISTRIBUTION/AVAILABILITY OF ABSTRACT: UNCLASSIFIED/UNLIMITED ☒ SAME AS RPT. ☒ DTIC USERS ☐

21. ABSTRACT SECURITY CLASSIFICATION: UNCLASSIFIED

22a. NAME OF RESPONSIBLE INDIVIDUAL: JOSEPH W. HAGER, Maj, USAF

22b. TELEPHONE NUMBER *(Include Area Code)*: 202-767-4933

22c. OFFICE SYMBOL: NE

DD FORM 1473, 83 APR — EDITION OF 1 JAN 73 IS OBSOLETE.

UNCLASSIFIED

SECURITY CLASSIFICATION OF THIS PAGE

Table of Contents

Section	Title	Page

INTRODUCTION

OVERVIEW.. 1
BACKGROUND.. 1
STATEMENT OF WORK... 2

TEST DESCRIPTION

LOS ALAMOS MESON PHYSICS FACILITY........................... 2
HARVARD CYCLOTRON LABORATORY................................ 4

DETECTOR DESCRIPTIONS

IMAGING TUBES... 4
PHOTODIODES... 15
BASIC DETECTOR OPERATION.................................... 18
JUNCTION PHOTODIODES.. 21
PHOTOEMISSIVE DETECTORS..................................... 24
RESULTS... 26
LAMPF TEST RESULTS.. 27
HARVARD CYCLOTRON TEST RESULTS.............................. 31
SYSTEM CONSIDERATIONS....................................... 43
SUMMARY... 52

REFERENCES.. 54

List of Figures

Figure No.	Title	Page
1	Neutral Particle Beam System	3
2A	Macro Pulse Mode	5
2B	Micropulse Mode	5
3	Test Configuration	6
4	Second Harvard Test Configuration	7
5	FW129 and FW130 Dimensions and Electrode Configuration	9
6	Sensitivity and Gain Characteristics	10
7	F130 Sensitivity and Gain Characteristics	12
8	F4012 Physical Dimensions	13
9	F4012 Configuration	14
10a	Silicon Avalanch Photodiode	17
10b	Avalanche Photodiode Electric Field	17
11	Planar Diffused p-n Junction Photodiode	19
12	Schottky Barrier p-i-n Photodiode	20
13	Charge Funneling	23
14	FW129 Temporal Response	28
15	FW130 Temporal Response	29
16	F4012 Temporal Response	30
17	FW129 Multiplier Phototube Response	32
18	FW129 Temporal Response	33
19	FW130 Multiplier Phototube Response	34
20	4012 Multiplier Phototube Response	35
21	30902E Avalanche Photodiode Response	36
22	30916E Avalanche Photodiode Response	37
23	30817E Avalanche Photodiode Response	38
24	SD-100-12-22-021 Photodiode Response	39
25	SD-100-12-12-021 Photodiode Response	40
26	PIN-10 Photodiode Response	41
27	Equivalent Noise Circuit	45
28	Tracker Acquisition Time	50
29	Tracker Signal-to-Noise	51

List of Table

Table No.	Title	Page
1	FW129 Characteristics	8
2	FW130 Characteristics	11
3	F4012 RP Characteristics	15
4	Avalanch Photodiodes Characteristics	16
5	Silicon Detector Corporation Photodiode Characteristics	18
6	United Detector Tech;nology, Inc. Pin-10 Characteristics	18
7	Slope and Arr	42
8	Visible Channel Noise Sources	46
9	Nominal Noise Voltages at Room Temperature	47
10	Star Tracker Current to Achieve a Signal-to-Noise Ratio of 5.5	49

ABSTRACT

The results of an experimental investigation into the interaction of protons, E = 318 MeV and 132 MeV, with selected multiplier phototubes and silicon photodiodes are presented. The devices were chosen because of their spaceborne applications and previous gamma ray, electron, and lower energy proton measurements. The energies are representative of those expected of particle beam weapons.

A discussion of the operation of each device and its expected response to protons is presented. Testing at Los Alamos Meson Physics Facility demonstrated the temporal response of multiplier phototubes to be nanoseconds but requires microseconds for decay. Another test at the Harvard Cyclotron Laboratory determined the transient response of these sensors to 132 MeV protons in the range of 10^5 to 2×10^8 P/cm^2 sec. The response was very nearly linear, but was slightly less for most devices. The radiation sensitivity of each device was calculated as expected. The multiplier phototubes were the least sensitive.

The results of these measurements were used to determine the effects of proton irradiation on system performance. Two systems were considered. One was a moderate resolution imaging system which uses photodiode sensors. The signal-to-noise of the system was calculated for varying radiation currents. The second system was a tracking instrument which uses an image dissector. The signal-to-noise and acquisition time were calculated.

Study of Spurious Sensitivity of Electronics in Space

INTRODUCTION

OVERVIEW

This document is the final report for AFOSR contract F49620-83-C-0153 titled, "Study in Spurious Sensitivity of Electronics in Space." It is the initial phase of an effort to characterize the effects of particle-beam weapons on electrical-optical systems by investigating basic processes. These measurements were two survey tests of photomultiplier tubes, an image dissector tube, and assorted silicon photodiodes frequently used in spaceflight applications. The detectors selected were an initial sample with which the ITT-Aerospace/ Optical Division was familiar.

Two different testing periods were used. The first at the Los Alamos Meson Physics facility was to determine the temporal response of photomultiplier tubes. Sufficient time was allowed between groups of pulses for complete recovery of the tubes. The second test was performed at the Harvard Cyclotron Laboratory. In this test the radiation induced response of photo multiplier tubes and photodiodes was measured as a function of beam flux. From these data the device response and beam induced dark current could be determined. These tests, in addition to providing useful information, were intended to point the direction for additional testing.

BACKGROUND

Passive electro-optical instrumentation is being used for a large variety of exatmospheric applications. These include, among others, tracking, threat sensing, surveillance systems, imaging, and meteorological applications. Spaceborne radiometric and sounding instrumentation developed and constructed by ITT-A/OD is providing and will continue to provide the bulk of the meteorological information for the National Oceanic and Atmospheric Agency (NOAA). These instruments are also monitored periodically by the military to support their weather mission.

The naturally occurring space environment is of concern to instrumentation on earth-orbiting satellites. The various types of radiation including gamma rays, x-rays, electrons, neutrons, protons, alpha particles, and heavy ions from trapped radiation, solar flares, and cosmic rays can cause permanent and transient effects in materials and devices which adversely affect complete systems. The extent of these problems is a constantly recurring question. The Electro-Optical Systems Department at ITT-A/OD regularly performs radiation analyses before choosing parts and materials. In addition, instrument performance in the ambient space radiation and nuclear blast environment is estimated.

Ballistic missile defense and ASAT and DSAT concepts has raised the possibility of particle beam weapons in space. These weapons can result in a radiation environment that is considerably different than that of naturally occurring radiation or even the nuclear blast environment. This is true whether the instruments are the target of the weapon or support for the weapon itself. Since many military systems require continuous operation or at the most millisecond recovery times during exposure to ionizing radiation, understanding the response of the instrumentation is essential.

ITT-A/OD has been considering the properties of an electro-optical counter measures system based on neutral particle streams. This countermeasures system will use a relatively low-power, low-flux, low-energy neutral particle stream that will generate sufficient noise in an electro-optical system to render it useless during at least the time the beam is on the system. More persistent and perhaps even permanent effects due to increased noise, false signals, logic upset, and even device burnout may also be present.

Figure 1 is a representation of such a spaceborne neutral particle beam system. The figure is general enough to describe both a weapons system and a covert surveillance jammer/countermeasures system. Differences occur in the system parameters and the resulting requirements of the subsystems. The jammer/countermeasures system is based on disabling an electro-optical pointing and tracking system at 1000 km using a defocused neutral particle beam. Preliminary estimates show these requirements are attainable with existing technology.

STATEMENT OF WORK

The thrust of this effort was to perform a preliminary survey of the effects of protons on sensitive electro-optical sensors used in space. The testing was in two segments. For the initial testing a few readily available devices were selected which do not require cooling and have high gain. These were photo multiplier tubes and an image dissector tube manufactured by ITT-A/OD's sister division the Electro-Optical Products Division. The temporal response of these tubes was measured at the Los Alamos Meson Physics Facility.

The second test measured the transient response of these same devices and photodiodes from RCA, Silicon Detector Corporation, and United Detector Technology. The tests were performed at the Harvard Cyclotron Laboratory.

TEST DESCRIPTION

LOS ALAMOS MESON PHYSICS FACILITY

The Los Almos Meson Physics Facility (LAMPF) is a three-stage linear proton accelerator with a length of 800m. It consists of a source and Cockcroft-Walton injector to accelerate protons to 750 kev, a drift tube linear accelerator to raise the energy to

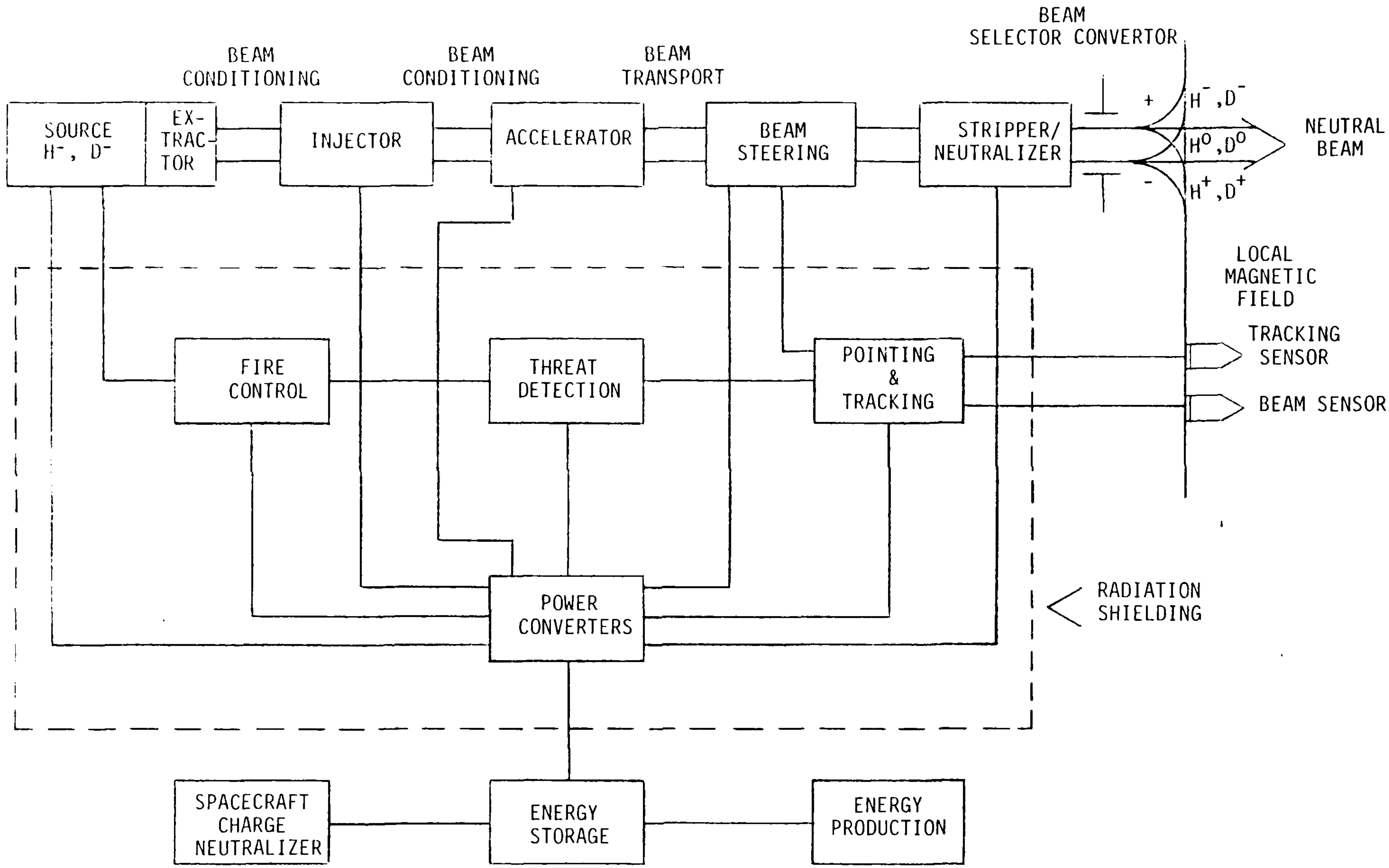

Figure 1. Neutral Particle Beam System

100 MeV, and a side-coupled-cavity linear accelerator to raise the energy to 800 MeV. The output energy is normally 800 MeV but is continuously variable between 100 and 800 MeV.

The pulse structure of the LAMPF accelerator normally consists of macropulses 720 μs long repeating at either 80 Hz or 120 Hz as shown in Figure 2A. Each macropulse is made up of micropulses each approximately 200 ps long containing $10^7 - 10^8$ protons separated by 4.97 ns. For this test the proton energy was 318 MeV; the time between micropulses was increased to 4.5 μs and the repetition rate was 8 Hz. The macropulse remained 720 μs long. The total charge in each micropulse was 10 ±5 pc. The average particle intensity in a micropulse was $3.1 \pm 1.5 \times 10^{17}$ protons/second. Each macropulse contained 60 micropulses 1600 ±800 pc or $1.0 \pm 0.5 \times 10^{10}$ protons. Figure 2B shows the beam structure used in the test. This beam is ideal for measuring the temporal response of a photomultiplier tube allowing it to recover partially between micropulses and completely between macropulses. The test configuration is shown in Figure 3.

HARVARD CYCLOTRON LABORATORY

The Harvard Cyclotron is a synchrocyclotron capable of accelerating protons to a maximum energy of 160 MeV. Degraders are used in the external beam to reduce proton energy as required, down to about 20 MeV. Energy resolution is typically 2 to 5 MeV for energies above 100 MeV and is 10 MeV for lower energies. The time structure of the external beam can be varied but consists typically of a 400 microseconds burst of protons every 10 milliseconds. Internal beam current is about 0.5 microamps. External beam current is variable from about 5 nanoamps down to a few protons per second. Beam diameter can be adjusted from less than 0.1 cm to a maximum of 30 cm.

For this test the proton energy was 132 MeV and the beam diameter was 5.0 cm to facilitate device placement. The test configuration is shown in Figure 3. The test equipment was as described above with the addition of a Keithley 619 Electrometer to measure the anode current.

Beam current and device current measurements were made independently. Multiple measurements were taken at each beam current. Because of variations in the cyclotron beam midway through the measurements, the test setup was changed so that the beam and device output currents were sampled at the same time was shown in Figure 4. This configuration allows for longer sample times and more strongly shows the correlation between the cyclotron beam variations and the device output.

DETECTOR DESCRIPTIONS

IMAGING TUBES

Three tube types were used in testing. Two were multiplier phototubes and one was an image dissector tube. All the tubes were manufactured by ITT-Electro-Optics Products Division.

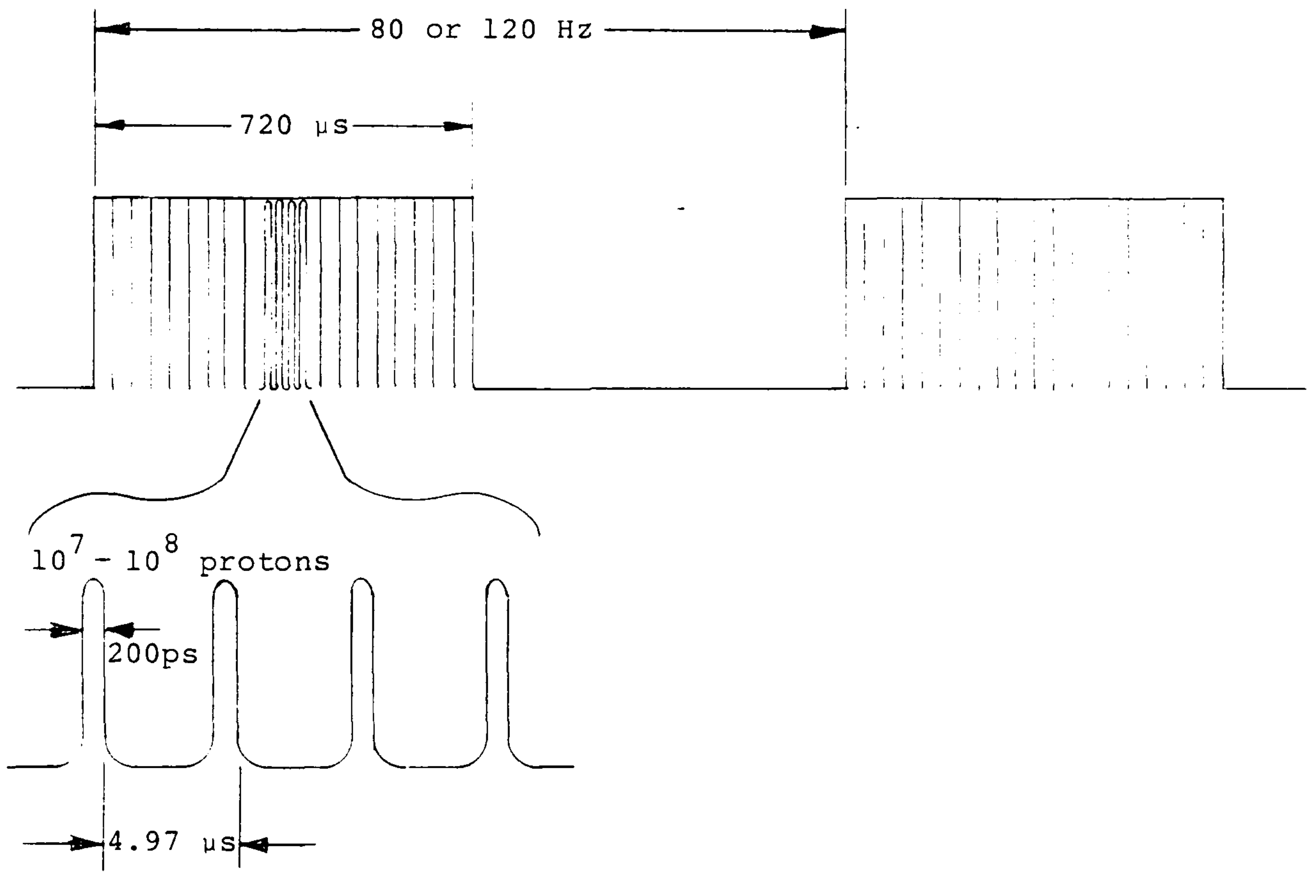

Figure 2A. Macro Pulse Mode

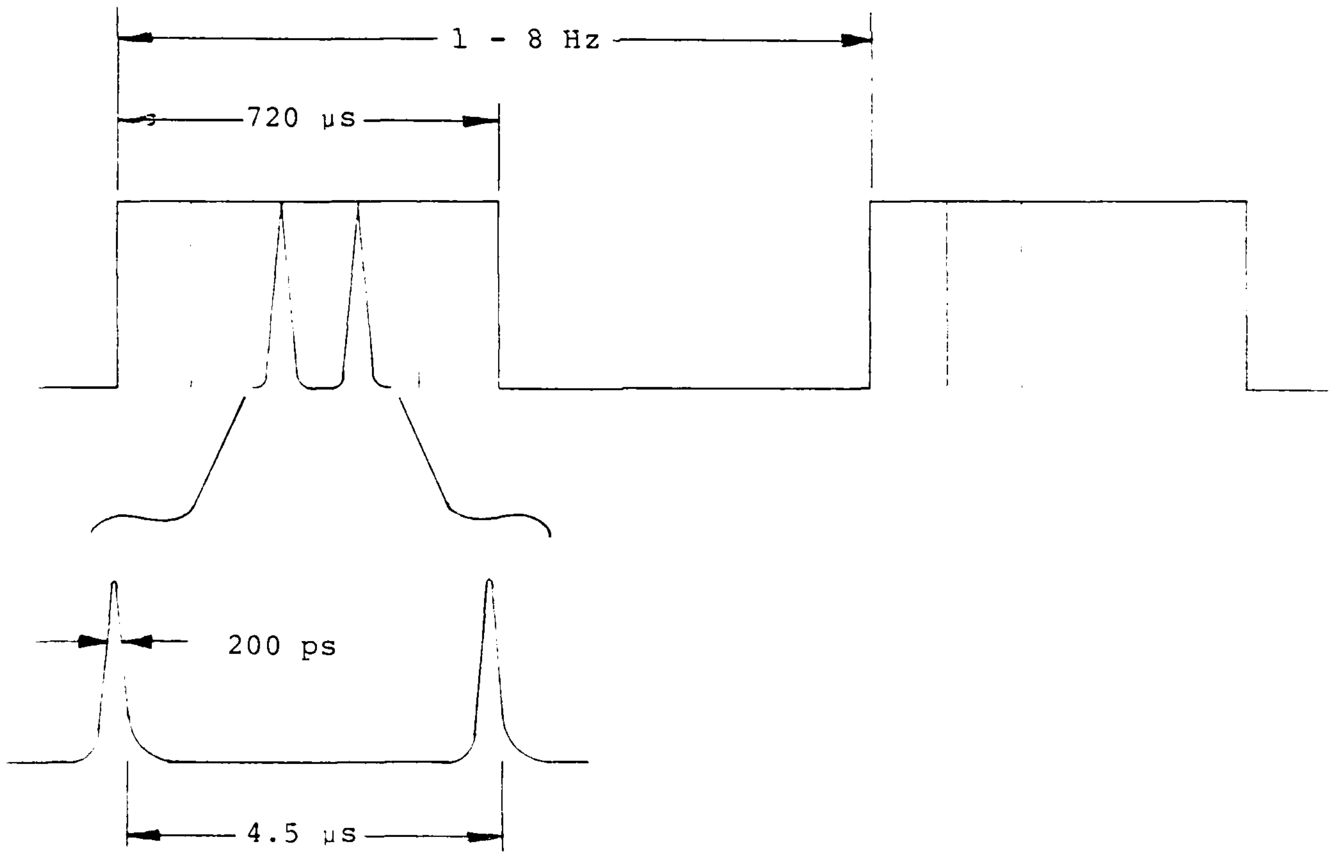

Figure 2B. Micropulse Mode

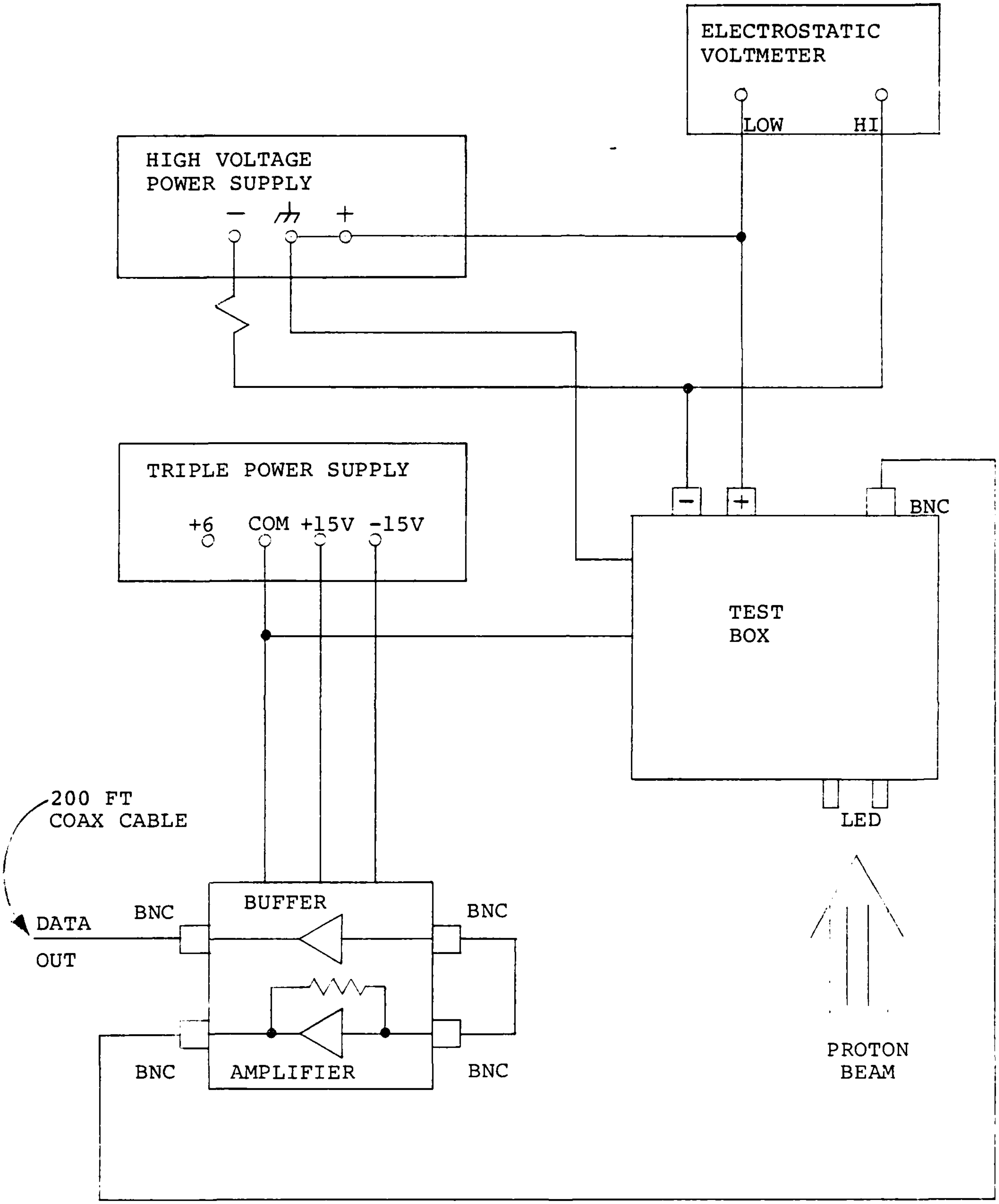

Figure 3. Test Configuration

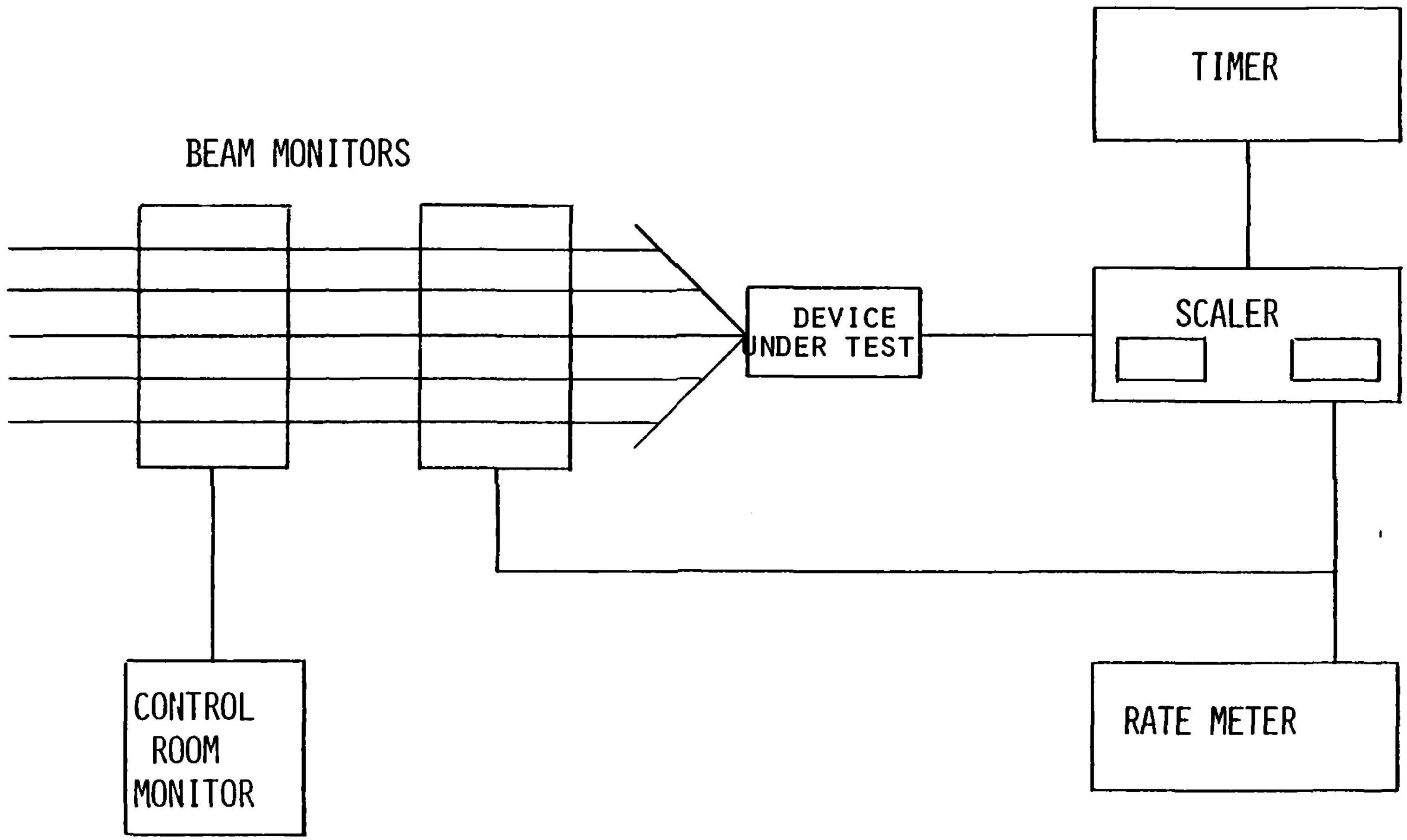

Figure 4. Second Harvard Test Configuration

Multiplier phototubes and image dissectors are photoemissive detectors in which radiation is absorbed by an alkali metal surface. This surface then emits photoelectrons which are collected by a dynode structure. Electron multiplication takes place and secondary electrons are produced at subsequent dynodes.

Multiplier phototubes are used in a variety of applications primarily because of their high gain and low noise compared to semiconductor devices. This allows the detection of very low level signals. In addition, the response time is very fast. Another advantage is the ability to construct large uniform detector surfaces which can be used for direct viewing or scanned for high spatial resolution (Ref 1).

The FW129 is a special purpose 16-stage multiplier phototube having an end-window type photocathode of restricted area with an individually calibrated S11-type spectral response. It has found particular application as a low noise optical tracking detector in non-contacting motion analysis systems. The FW129 may be used as an electronic star tracker for guidance and control of space vehicles. An electrostatically focused electron lens system with a defining aperture in the electron image plane is incorporated between the photocathode and the first dynode to limit the effective photocathode area. This feature reduces the equivalent noise input by minimizing collected thermionic emission current and ion feedback at the same time maintaining high collection efficiency in the effective photocathode area. Figure 5 shows the physical dimensions of the FW129 and the electrode configuration. Figure 6 displays the sensitivity and gain characteristics as a function of applied voltage. Table 1 is a list of pertinent parameters.

Table 1. FW129 Characteristics

Face Plate Material	7056 Borosilicate glass
Face Plate Thickness	1.14 $\pm$0.05 mm
Photocathode	Semitransparent S11
Wavelength of Maximum Response	420 $\pm$50 nm
Dynode Substrate	Ag - Mg
Dynode Emitting Surface	MgO
Typical Gain @ 1800V	5×10^6
Typical Luminous Sensitivity (2854K)	200 A/lM
Peak Radiant Sensitivity @ 420 nm	8.1×10^4 A/W
Typical Node Dark Current	10 nA
Max Dark Current	50 nA
Cathode Peak Quantum Efficiency	9%
Peak Anode Current	0.5 mA

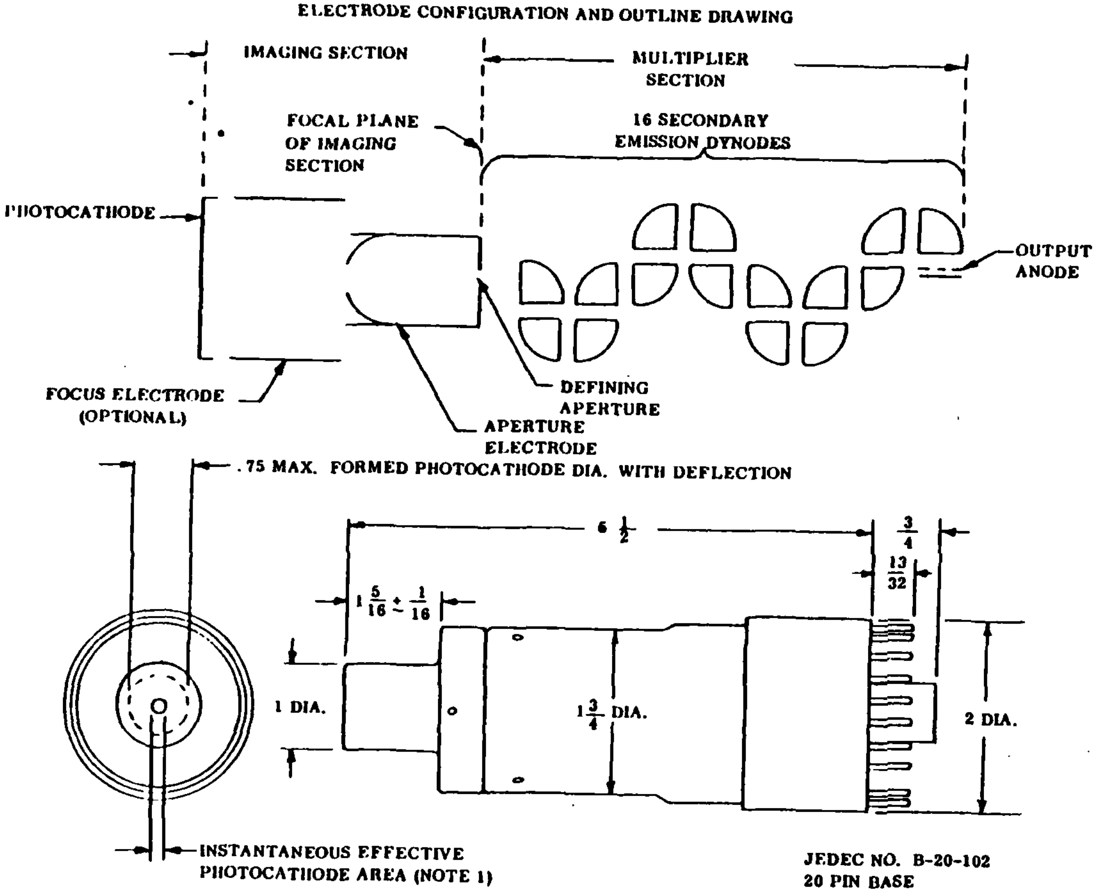

SOCKET CONNECTIONS

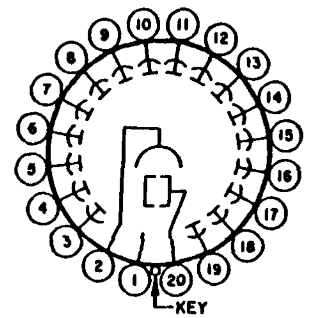

Pin 1	No Connection	Pin 11	Anode
Pin 2	Photocathode	Pin 12	Dynode No. 16
Pin 3	Dynode No. 1	Pin 13	Dynode No. 14
Pin 4	Dynode No. 3	Pin 14	Dynode No. 12
Pin 5	Dynode No. 5	Pin 15	Dynode No. 10
Pin 6	Dynode No. 7	Pin 16	Dynode No. 8
Pin 7	Dynode No. 9	Pin 17	Dynode No. 6
Pin 8	Dynode No. 11	Pin 18	Dynode No. 4
Pin 9	Dynode No. 13	Pin 19	Dynode No. 2
Pin 10	Dynode No. 15	Pin 20	Aperture Electrode

Figure 5. FW129 and FW130 Dimensions and Electrode Configuration

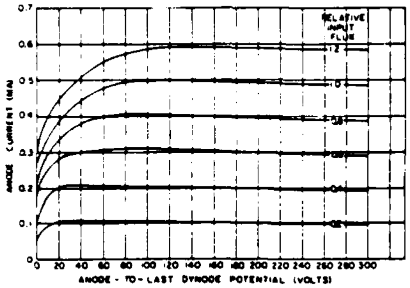

ANODE CHARACTERISTIC CURVES

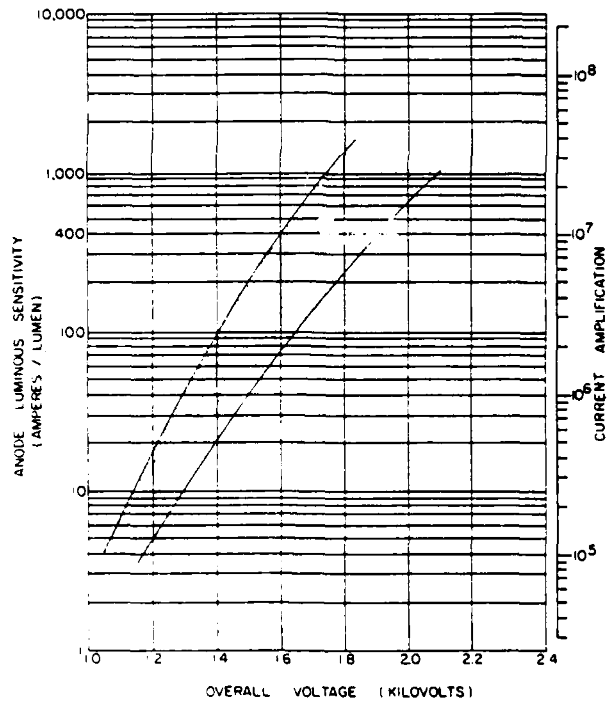

SENSITIVITY AND GAIN CHARACTERISTICS

Figure 6. Sensitivity and Gain Characteristics

The FW130 is a special purpose 16-stage multiplier phototube having an end-window type photocathode of restricted area with a calibrated S20 spectral response. It has found particular application as a low noise detector for stellar observations and laser receivers when the input radiant flux can be confined to a small area. The FW130 may be used as an electronic star tracker for guidance and control of space vehicles.

An electrostatically focused electron lens system with a defining aperture in the electron image plane is incorporated between the photocathode and the first dynode to limit the effective photocathode area. This feature reduces the equivalent noise input by minimizing collected thermionic emission current and ion feedback, at the same time maintaining high collection efficiency in the effective photocathode area. Figure 5 shows the physical dimensions and the electrode configuration of the FW130. The sensitivity and gain characteristics are shown in Figure 7. Table 2 summarizes the characteristics of the FW130.

Table 2. FW130 Characteristics

Face Plate Material	7056 Borosilicate glass
Face Plate Thickness	1.1 $\pm$0.05 mm
Photocathode	Semitransparent S20
Wavelength of Maximum Response	420 $\pm$50 nm
Dynode Substrate	Ag - Mg
Dynode Emitting Surface	Mg
Typical Gain @ 1800V	5×10^6
Typical Luminous Sensitivity (2854K)	800 A/lM
Peak Radiant Sensitivity @ 420 nm	3.25×10^5 A/W
Typical Node Dark Current	2 nA
Max Dark Current	15 nA
Cathode Peak Quantum Efficiency	12%
Peak Anode Current	0.5 mA

The F4012 is a magnetically focused magnetically deflected image dissector. Figures 8 and 9 show the physical dimensions and configuration of the image dissector. The F4012RP is used in applications which require very low dark rates and excellent mechanical stability. The salient features are an inherently high resolution (determined primarily by the size and shape of the aperture), nonstorage (allowing random or variable scan rates without changes in the signal amplitude), and reliable operation because of simple rugged construction and lack of a thermionic cathode. In addition, the F4012 has a linear range of several orders of magnitude. Table 3 lists the characteristics of the F4012.

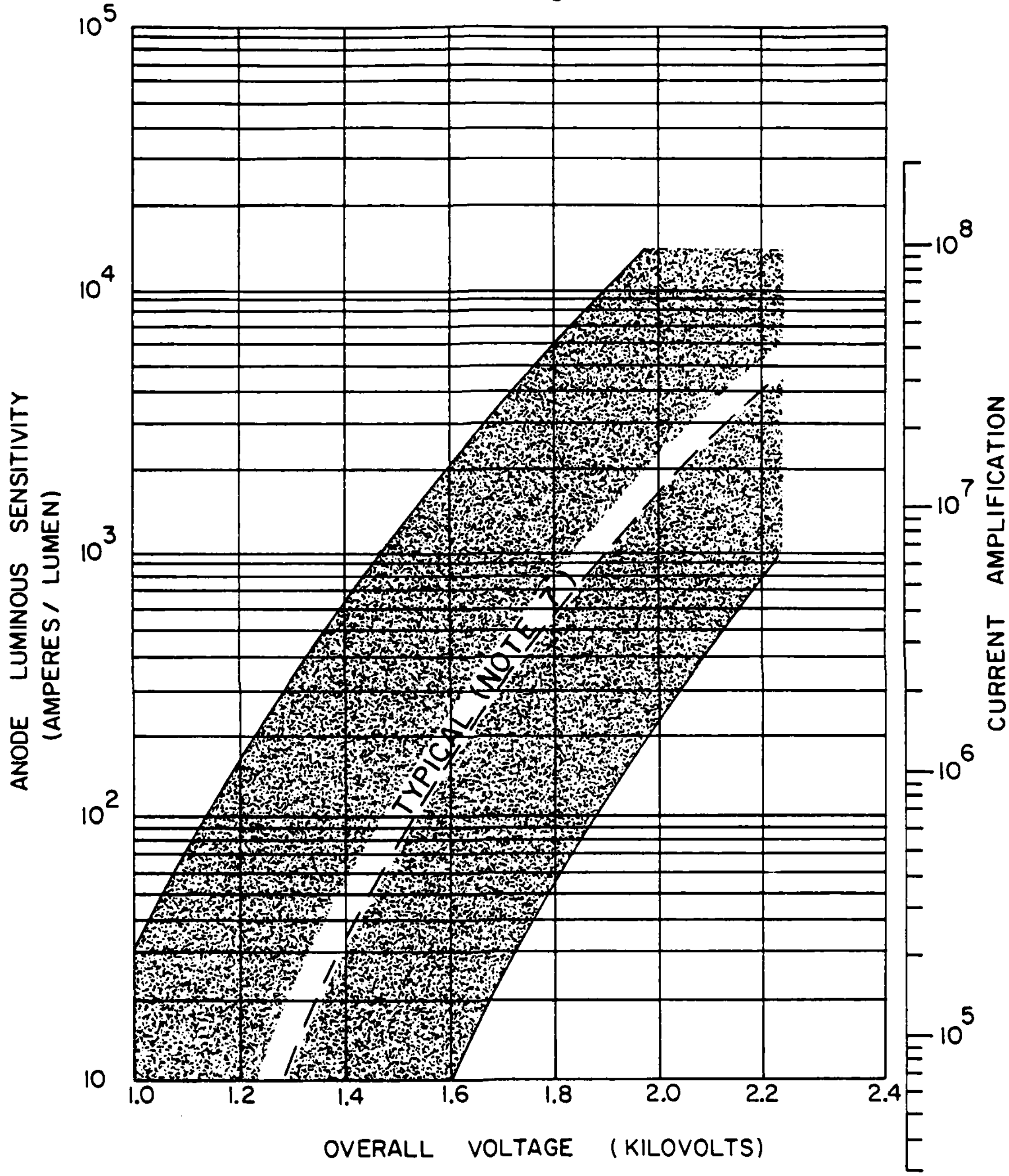

Figure 7. F130 Sensitivity and Gain Characteristics

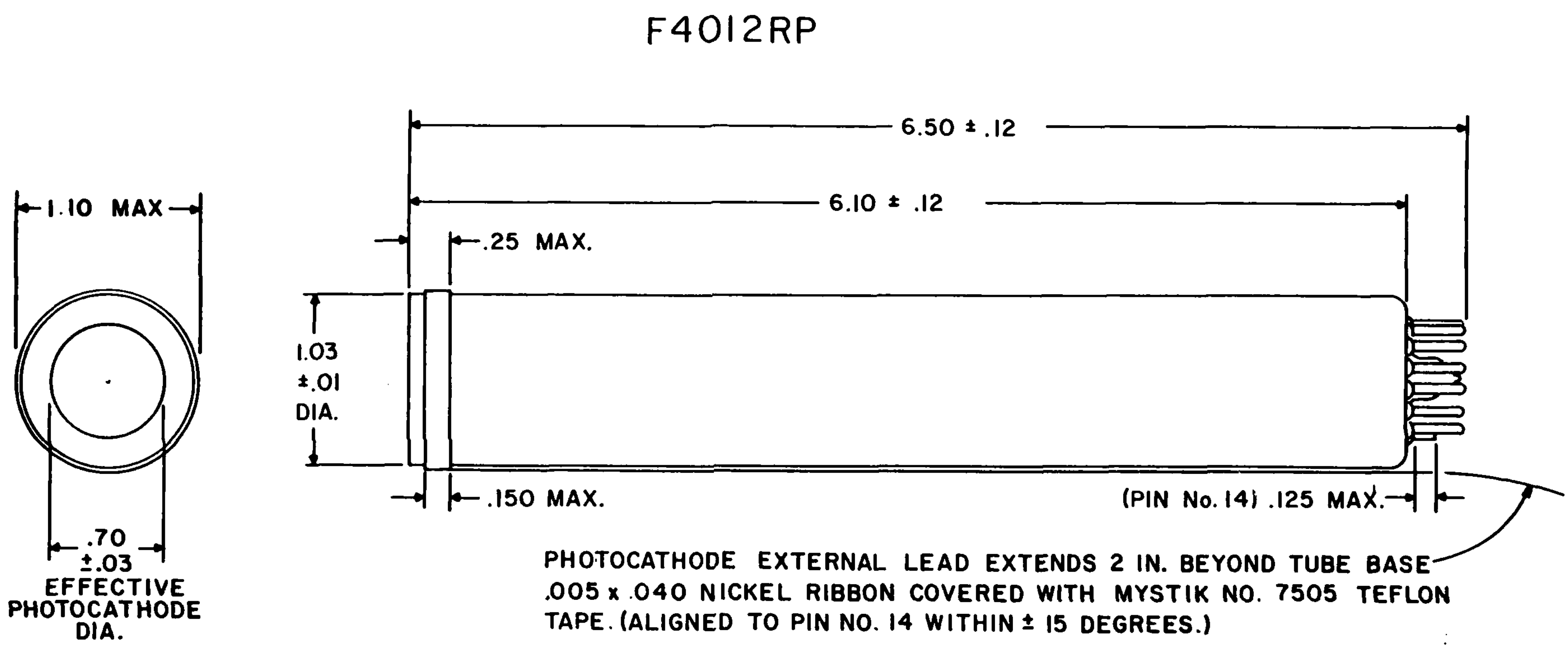

Figure 8. F4012 Physical Dimensions

F4012, F4012RP

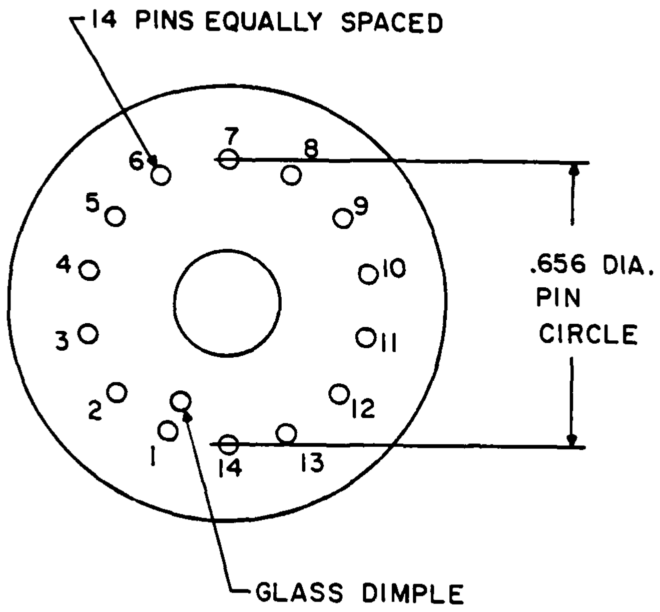

PIN	ELEMENT
1	DRIFT TUBE
2	DYNODE 8
3	DYNODE 1
4	DYNODE 2
5	DYNODE 3
6	DYNODE 10
7	INTERNAL CONNECTION
8	DYNODE 11
9	ANODE GUARD RING
10	ANODE
11	DYNODE 12
12	DYNODE 9
13	DYNODE 7
14	KEY PIN (CLIPPED)

FLYING LEAD – PHOTOCATHODE

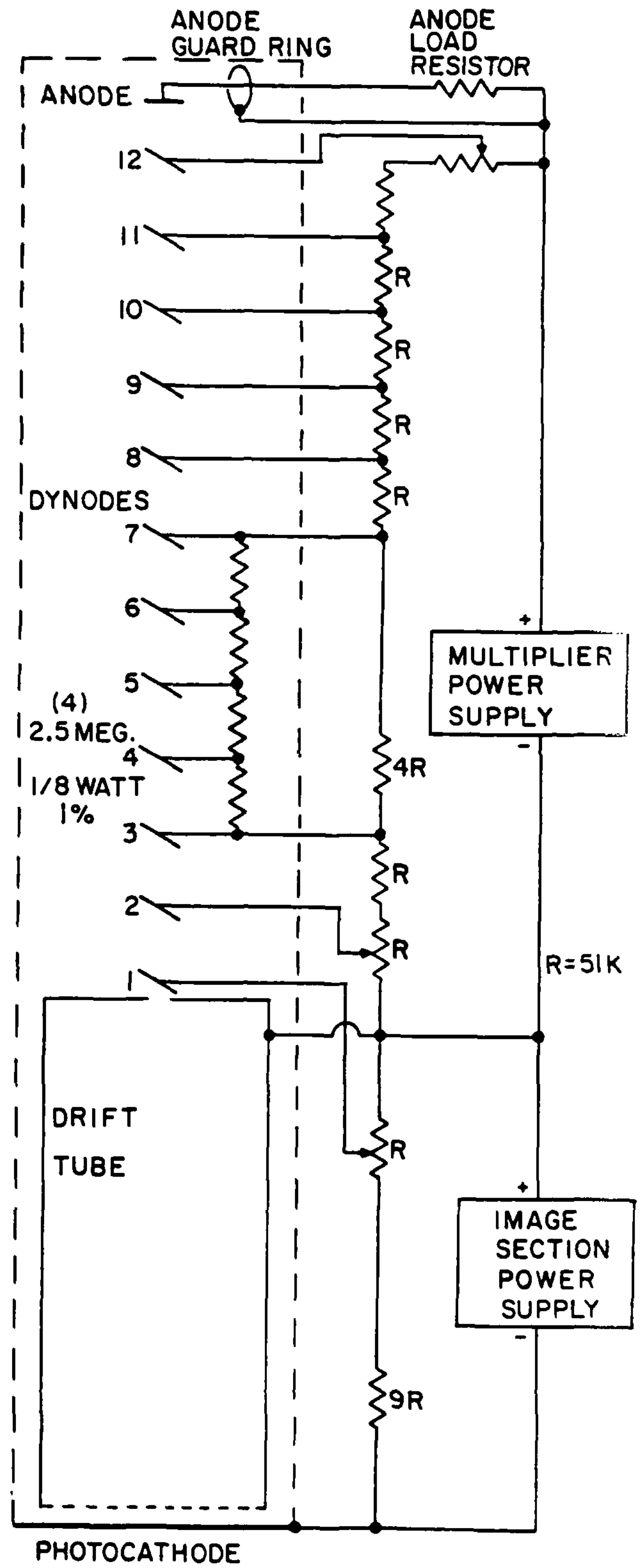

Figure 9. F4012 Configuration

Table 3. F4012 RP Characteristics

Photocathode	Semitransparent MA-2
Face Plate Material	Borosilicate glass
Face Plate Thickness	0.254 $\pm$0.013 mm
Wavelength of Maximum Response	550 nm
Dynode Substrate	Ag - Mg
Typical Gain @ 1800V	5×10^5
Typical Luminous Sensitivity (2854K)	125 A/lM
Peak Radiant Sensitivity @ 420 nm	2.5×10^4 A/W
Typical Node Dark Current	1×10^{-10} A
Max Dark Current	5×10^{-9} A
Peak Anode Current	0.5 ma

PHOTODIODES

Many types of p-n junction detectors are available for a large variety of purposes. Some parameters of interest when selecting a detector are spectral response, leakage current, temporal response, uniformity, responsivity, size, ease of manufacture, etc. The problem in an initial investigation is to pick detectors which are representative of the many devices available. Silicon photodiodes were chosen because of the vast amount of work which has been performed and because of the many years they have used in the spaceborne instrumentation designed and constructed by ITT-A/OD.

Three RCA avalanche photodiodes were selected for testing. Two are general purpose devices which differ mainly in area. One is a high-speed wide-bandwidth device. Two planar diffused diodes were purchsed from Silicon Detector Corporation. One was a medium frequency device designed to be operated photovoltaicly. The second was a high-frequency device designed to be operated photoconductively. The final detector selected was a p-i-n photodiode with a Schottky barrier manufactured by United Detector Technology, Inc. These devices represent only a few of the many silicon photodiodes by various manufacturers which are available.

The avalanche photodiode is of considerable interest in fiber optics communications. By using a high-electric field it has an internal gain to boost the photocurrent signal. This maximizes the signal-to-noise ratio of very weak optical signals. The electric field in an avalanche photodiode accelerates the minority carriers in the depletion region. Additional carriers are produced by impact ionization resulting in signal multiplication.

Avalanche photodiodes are currently not widely used in space. According to references 1 and 2 they are better selections than p-i-n devices in systems with low-power optical signals and large bandwidths. Their case is limited by the large bias required, radiation sensitivity, and the availability of photoemissive detectors.

Radiation sensitivity is due primarily to operation with a bias very near their breakdown voltage. Radiation, temperature changes or electric fluctuations can cause large currents to be produced which can destroy the device (Ref 2).

Figure 10a shows the general structure of an RCA avalanche photodiode. A p-type substrate material is used. The p and n diffusions are boron and phosphorus, respectively. An electric field profile for the avalanche photodiode is shown in Figure 10b. Reverse bias is applied until the depletion layer of the p-n junction just reaches the low concentration region. A small additional applied voltage causes the depletion layer to increase rapidly out to the P+ surface while the field throughout increases slowly. When electromagnetic radiation impinges on the P+ surface, electrons are swept to the high-yield region where multiplication occurs. The holes produced in the high-field region traverse the region to the P+ surface producing the multiplied signal.

RCA C30916E and C30817 are general purpose silicon avalanche photodiodes. Their useful spectral response range is from 400 to 1100 nanometers. The responsivity of these devices is independent of modulation frequency up to about 200 MHz. The RCA C30902E avalanche photodiode is a high-speed wide bandwidth device. The responsivity of the diode is independent of modulation frequency up to 800 MHz. These devices are useful for laser detection, ranging, optical communications, high-speed switching and transit time measurements. Characteristics of these avalanche photodiodes are shown in Table 4.

Table 4. Avalanche Photodiodes Characteristics

CHARACTERISTIC	C30817	C30902E	C30916E
Useful Area	0.5 mm^2	0.2 mm^2	1.77 mm^2
Useful Diameter	0.8 mm	0.5 mm	1.5 mm
Typical Dark Current	5×10^{-8}A	1.5×10^{-8}A	1×10^{-7}A
Typical Breakdown Voltage	375V	225V	390V
Gain	120	150	80
Responsivity @ 900 nm	75 A/W	65 A/W	50 A/W
Quantum Efficiency @ 900 nm	85%	60%	85%
Typical Rise and Fall Times	2 ns	0.5 ns	3 ns
Thickness of π Region	0.11 mm	0.030 mm	0.11 mm

Two general purpose silicon diodes were purchased from the Silicon Detector Corporation. One was designed to be operated photovoltaicly. In this mode collection of carriers will take place throughout the depletion region and for approximately one minority carrier diffusion length into the undepleted region. The highly doped layer on top does not make a significant contribution to the photocurrent because of recombination at the surface and the limited hole diffusion length. Junction detectors may be operated with a reverse bias in a photoconductive mode. This has the effect of increasing the

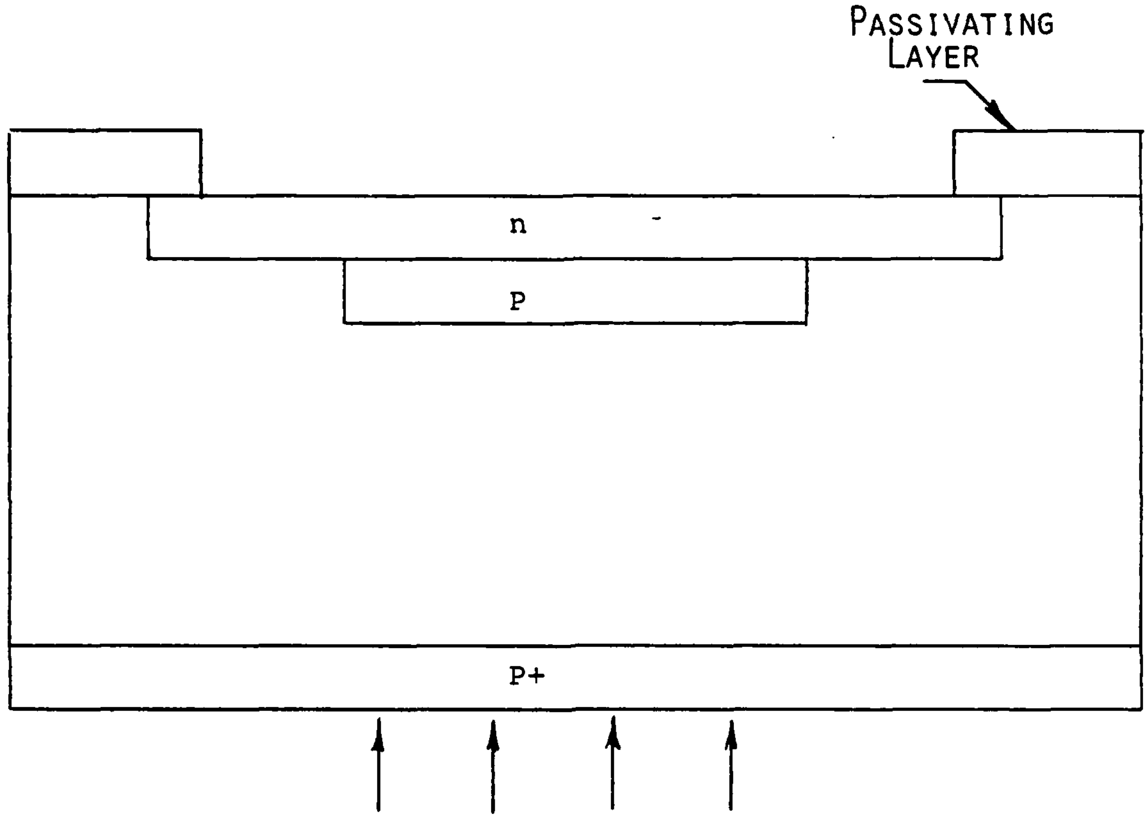

Figure 10a. Silicon Avalanche Photodiode

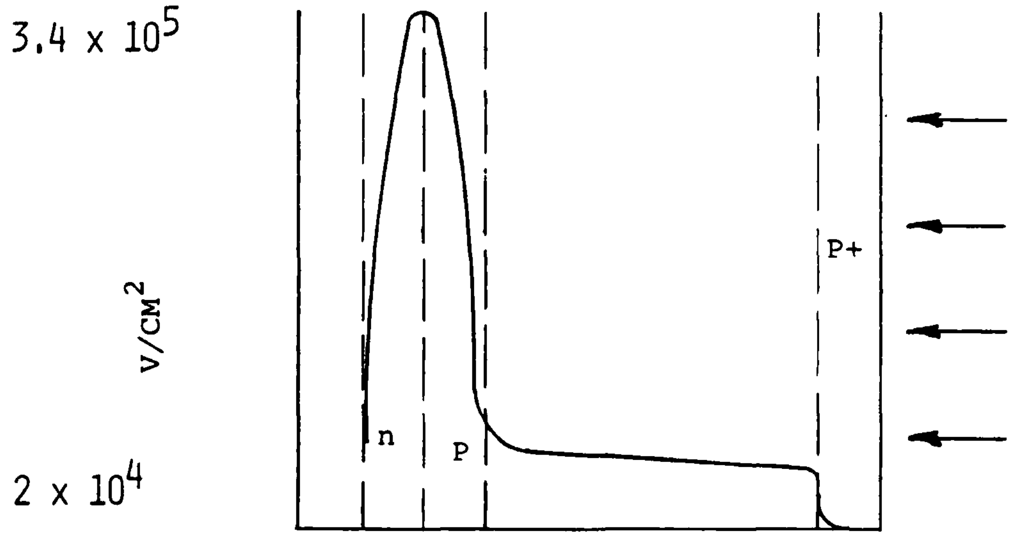

Figure 10b. Avalanche Photodiode Electric Field

frequency response of the detectors but also increases the noise (Ref. 4). A idealized diagram of a p-n junction photodiode is shown in Figure 11. The properties of the two Silicon Detector Corporation photodiodes are described in Table 5.

Table 5. Silicon Detector Corporation Photodiode Characteristics

Characteristic	SD-100-12-12-021	SD-100-12-22-021
Active Area	5.1 mm^2	5.1 mm^2
Responsitivity @ 900 nm	0.5 A/W	0.55 A/W
Typical Dark Current	0.75 na	105 na
Max Linear Output Current	0.42 ma	0.18 ma

A silicon p-i-n diode with schottky barrier was purchased by United Detector Technology, Inc. Figure 12 is a diagram of the construction. The major features are the nearly intrinsic region and the schottky barrier. The nearly intrinsic region is only lightly doped with a resistivity of 10 to 100,000 ohm-cm. The p and n region resistivities are considerably less tha 0.1 ohm-cm. In the p-i-n photodiode an applied voltage produces an electric field which extends across the intrinsic region. The optical photons are absorbed in the space charge region producing a diode with small series resistance, fast response, increased responsitivity and better linearity.

The schottky barrier is formed by a thin transparent layer of gold that is evaporated on an intrinsic region. The junction is formed at the gold-intrinsic region boundary when a potential is applied. When a photon is absorbed, the minority carrier is swept to the junction and the majority carrier is swept to the ohmic contact. This device has no heavily doped "dead" region at the top and is, therefore, able to detect shorter wavelength light than p-n or p-i-n photodiodes. Typical detector characteristics are shown in Table 6.

Table 6. United Detector Technology, Inc. Pin-10 Characteristics

Responsivity @ 850 nm	0.3 A/W
Typical Dark Current	0.5 μA
Active Area	1.25 cm^2
Active Diameter	1.26 cm
Risetime	10 ns
Maximum Current	10^{-3} W

BASIC DETECTOR OPERATION

This discussion will cover the very basics of detector operation. Many books, papers, and manufacturer's notes cover these topics in as much detail as desired (e.g. references 5, 6, 7, and 8). In addition, radiation effects will be discussed.

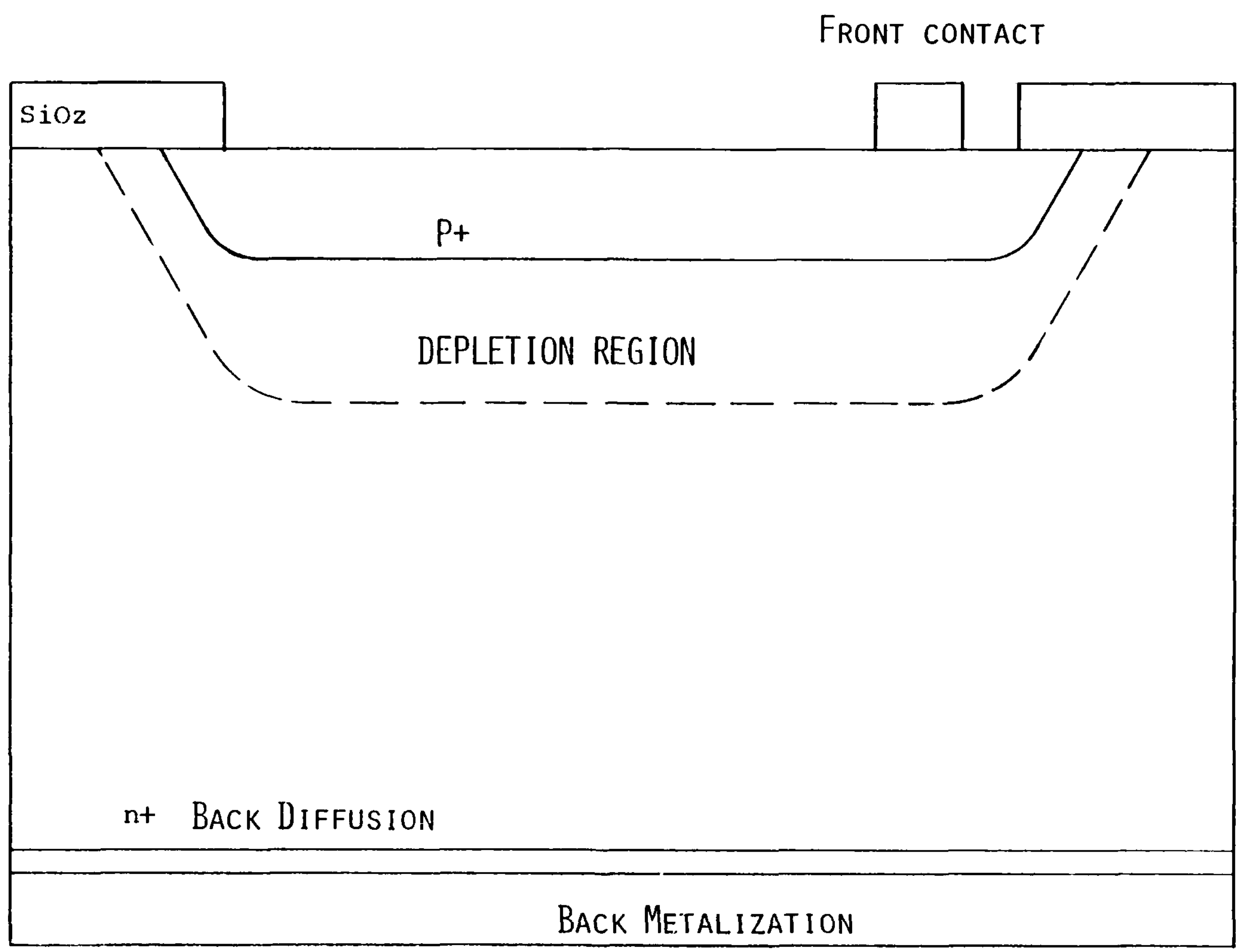

Figure 11. Planar Diffused p-n Junction Photodiode

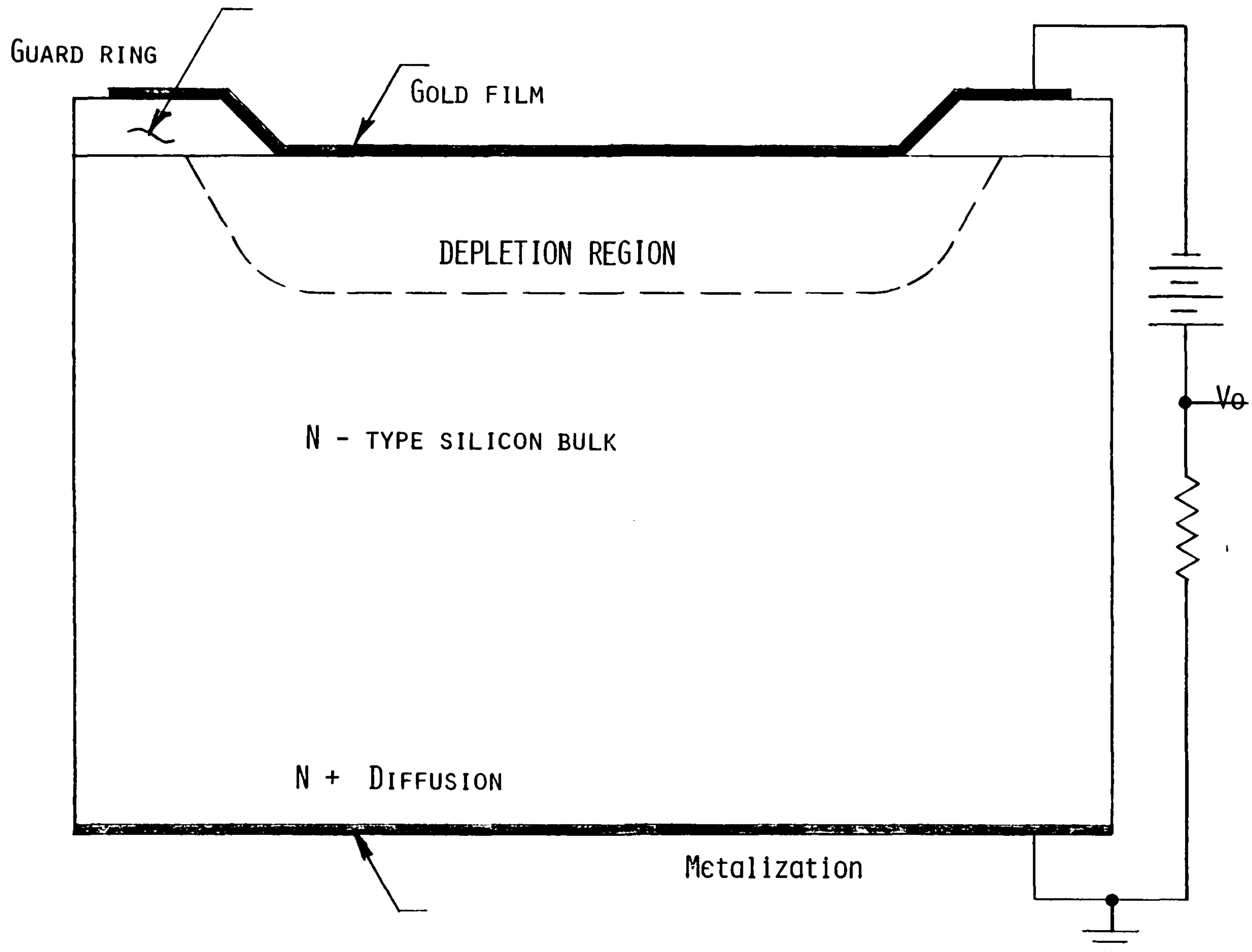

Figure 12. Schottky Barrier p-i-n Photodiode

JUNCTION PHOTODIODES

A junction photodiode consists of a p-n junction formed by various methods such as bulk doping, impurity diffusion, or growth of an epitaxal layer of one type upon a substrate of another type. Even without an external bias, a potential forms across the junction as electrons and protons diffuse. Incident photons of sufficient energy produce electron-hole pairs in the depletion region that are separated by the electric field at the junction. This is one component of the photocurrent. For monochromatic photons incident on a p-n junction the generation rate in a thickness x is given by:

$$R = N\alpha e^{-\alpha x} \qquad (1)$$

where N is the incident photon flux; α the optical absorption coefficient; and x is the distance into the device (Ref. 9). On integrating from zero to the depletion depth w, this expression becomes:

$$R = N(1-e^{-\alpha w}) \qquad (2)$$

For particles that penetrate completely through the device, this expression is simplified to:

$$R = g_o\dot{\gamma} \qquad (3)$$

where g_o is the number of electron-hole pairs produced per unit volume per unit radiation dose and $\dot{\gamma}$ is the dose rate. Note the difference between the generation rate for photons given in equation 2 and the uniform generation rate given in equation 3. g_o can be found from the energy required to produce one electron-hole pair (3.6 eV in silicon) and the density of the material.

$$g_o = 6.25x10^{13}(eV/g\text{-}rad)\rho E \qquad (4)$$

where ρ is the density and E is the energy to produce one electron hole pair. The primary drift current density for a radiation pulse which is long compared to the carrier lifetime is given by:

$$j_p = eRW = eg_o\dot{\gamma}W \qquad (5)$$

where W is the depletion layer width.

The second component of the photo current is generated within one diffusion length of the depletion layer. This component will diffuse to the depletion region and be collected later than the prompt current. For particles passing completely through the device this can be written as:

$$j_d = eR(L_n+L_p) \qquad (6)$$

where L_p is the hole diffusion length and L_n is the electron diffusion length. These minority carrier diffusion lengths can be related to the minority carrier lifetime by:

$$L = (D_{n,p}\tau_{n,p})^{1/2} \qquad (7)$$

where D is the diffusion constant and τ is the minority carrier lifetime.

One of the two terms in equation 6 can usually be ignored due to the construction of a photodiode. A thin heavily doped layer (Figure 11) is usually exposed to the incident light. The photocurrent generated in this thin top surface will make little contribution because of surface recombination and short minority carrier diffusion lengths (Ref. 2).

Equations 5 and 6 assume a radiation pulsewidth and current measured at a time that is long compared to the carrier lifetime. For a time short compared to the carrier lifetimes reference 10 shows that:

$$j_d = eR[W+L_n \operatorname{erf}\,(t/\tau_n)^{1/2}) + L_p \operatorname{erf}\,(t/\tau_p)^{1/2}] \qquad (8)$$

In addition to the drift current from the depletion region, two more sources of prompt photocurrent may also be present. One is from the terminally generated leakage current which is given by:

$$j_\ell = \frac{enW}{\tau} \qquad (9)$$

where τ is the effective liftime in the depletion region and n is the intrinsic carrier density (Ref. 9). The second method is called charge funneling shown in Figure 13. The field lines in the diode are distorted by the intense plasma produced when an ion passes through. This causes a very fast collection of charge from beyond the depletion region which can increase the charge collection by two to ten times (Ref. 11 and 12).

To obtain a rapid response from a photodiode it is desirable to decrease the component due to diffusion which depends on large diffusion lengths and therefore long minority carrier lifetimes (Ref. 2). Using a p-i-n configuration (Figure 12) reduces the diffusion component and increased the prompt photocurrent. When a reverse bias is applied the intrinsic region becomes part of the depeletion region. Most of the photons are then absorbed in the depletion region.

In the Schottky barrier photodiode the junction is formed at the gold intrinsic layer interface. Operation is similar to p-n and p-i-n photodiodes.

This discussion has so far only considered ionization as a method of transferring energy from an energetic proton to a detector. Reference 13 states that about 3.6 out of every 10^5 incident 40 MeV protons participate in a nuclear reaction in 10 μm of silicon. In this manner a large amount of energy can be deposited within a small volume compared to electrons or gamma rays (Ref. 14).

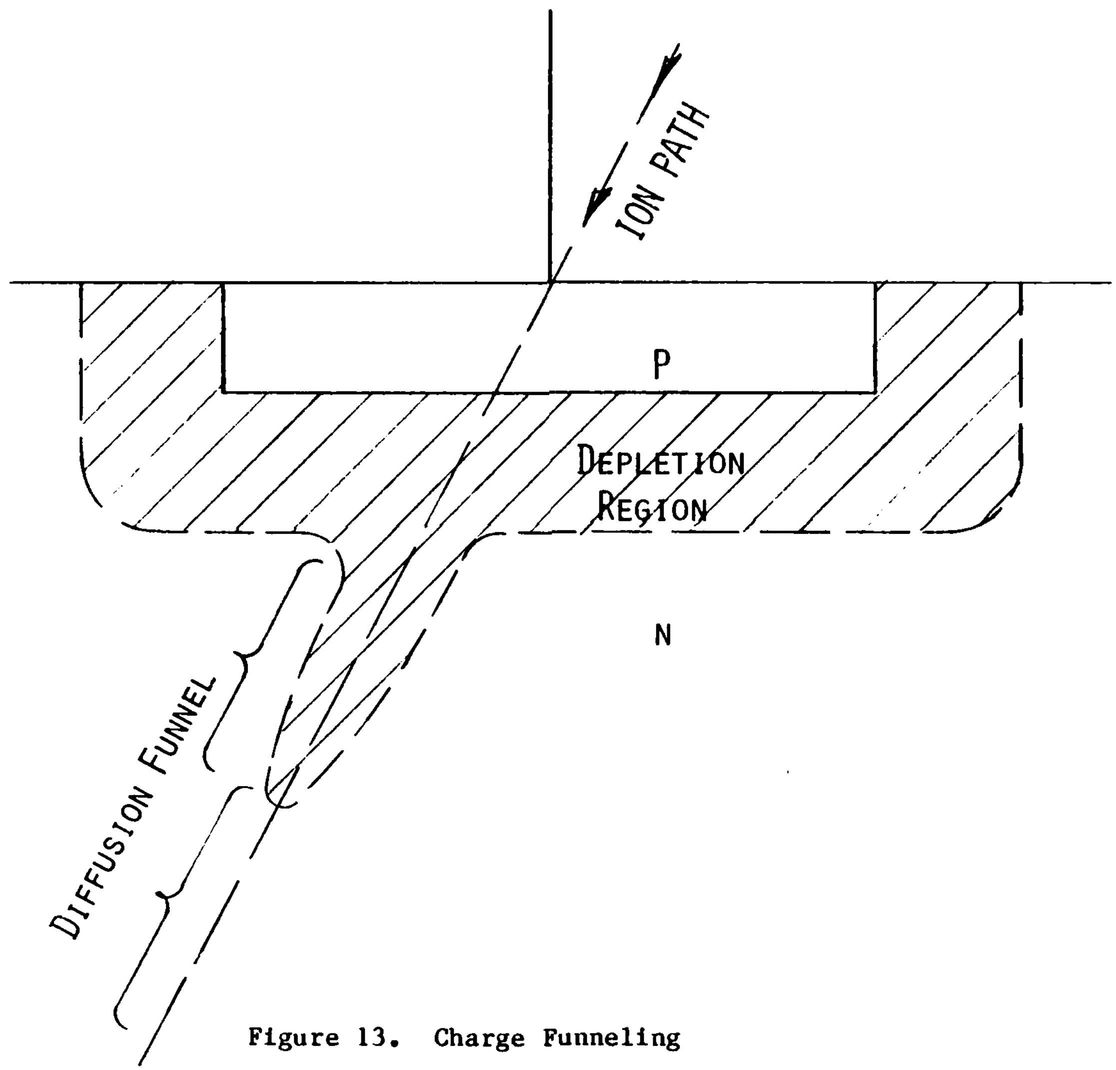

Figure 13. Charge Funneling

Following a nuclear reaction ionization effects are still the mechanism of energy transfer. This is done in three possible ways (Ref. 13 and 15):

1. Silicon recoils from elastic scattering.
2. Nuclear reactions producing alpha particles.
3. Nuclear reactions producing heavy nuclear recoil

In addition to the references already cited, references 16 and 17 discuss nuclear reactions:

PHOTOEMISSIVE DETECTORS

In photoemissive detectors such as the photomultiplier tubes and image dissector tube used during these tests, an incident photon is absorbed by a surface. Photoemission takes place by absorption of a photon giving energy to an electron. The electron moves toward the edge of the material and if it has sufficient energy escapes over the potential barrier at the surface. Energy losses take effect at every point. Much of the light is host by reflection and the electrons lose energy on collisions with other electrons in the metal. If the energy of the photon is greater than the work function of the surface electrons are emitted with a maximum energy given by:

$$E = hc/\lambda - \phi \qquad (10)$$

where E is the electron energy; h is Plank's constant; λ is the photon wavelength; c is the speed of light and ϕ is the work function of the surface. The photocurrent is given by:

$$I_c = (1-r)\ \eta e\phi\ \lambda/hc \qquad (11)$$

where r is the reflectance; η is the quantum efficiency; and ϕ is the incident flux. Photoemissive devices have the advantages of greater sensitivity, higher temporal resolution, and higher spatial resolution than solid-state devices.

Even when a photo multiplier tube is in complete darkness a current flows. This dark current is caused by ohmic leakage, thermonic emission, and regenerative effects (Ref. 8). Thermonic emission comes mainly from the photocathode and to a lesser extent from the dynode surfaces. The current density can be found from Richardson's equation:

$$j = \frac{4\pi emk^2T^2}{h^3} \exp\ (-\phi/kt) \qquad (12)$$

where e is the electron charge; m the electron mass; k Boltzman's constant; h Plank's constant; and T the absolute temperature. Regenerative effects include dynode glow, glass charging, and after pulsing.

Electrons that are emitted from the cathode encounter the dynodes. Those with sufficient energy cause the emission of secondary electrons from the dynodes in a fashion very similar to photons hitting the cathode. In this case electrons interact with electrons rather than photons interacting with electrons. The emission yield increases with incident electron energy if the secondary electrons are produced near the surface. As the incident electron energy increases the number of secondary electrons increase but they are produced deeper and more are lost.

Equation 11 can be written:

$$I_c = R_c \phi$$

where R is the responsivity. Not all the electrons leaving the photocathode will reach the first dynode and the anode current can be written (Ref. 18):

$$I_a = \phi R_c \xi_o (\delta\xi)^n \quad (13)$$

where ξ_o is the collection efficiency for the first dynode; ξ is the efficiency for subsequent dynodes; δ is the electron amplification by secondary emission, and n is the number of dvnodes. The anode responsivity is:

$$R_a = R_c \xi_o (\delta\xi)^n \quad (14)$$

where $\xi_o(\delta\xi)^n$ is called the gain (G).

The noise can be found by assuming that the incident flux is made up of photons whose distribution can be described by Poisson statistics. Reference 18 shows this can be described by a current given by:

$$\begin{aligned} I_n^2 &= 2eI_c \; \delta_n^{2n} \; \Delta f \; \delta/\delta{-}1 \\ &= 2eI_a \; \delta^n \; \Delta f \; \delta/\delta{-}1 \end{aligned} \quad (15)$$

were Δf is the bandwidth given by the inverse of twice the sample time. The signal-to-noise ratio is:

$$S/N = I_a/I_n = I_a/(2eI_a kG\Delta f)^{1/2} \quad (16)$$

In both photoemission and secondary emission there is a lag between the time the photon or electron impinges on the material and the time the secondary electron is emitted. Also, it takes some time for the secondary electrons to reach the surface. This time is one the order of 10^{-13} to 10^{-14} second. Therefore, the response time of the photomultiplier tube is determined by the time of flight of the electrons (~ tens of nanoseconds).

Numerous investigations, both experimental and theoretical, have been made of radiation effects in photomultiplier tubes (Ref. 19-23). The major effect of ionizing radiation reported in these references is the production of photons in the tube window by Cerenkov radiation and luminescence. Reference 22 identifies secondary electron emission and secondary photoemission (bremsstrahlung) as two other possible sources. All references found that the response was linear with increasing flux.

Cerenkov radiation is not a factor in the measurements discussed here which used 132 MeV protons with a β of 0.48. Cerenkov radiation in glass occurs only for β greater than 0.67 or 330 MeV for protons.

Fluorescence involves the excitation of the material in the faceplate and the subsequent release of a photon. Reference 24 gives the average number of photons per unit path length per event by:

$$N_{FL} = \varepsilon \; (dE/dx) \qquad (17)$$

where ε is the photon yield per MeV and dE/dx is the stopping power of the matrial. dE/dx is roughly independent of energy and depends on the square of the charge. ε is much harder to determine because of the broad spectral bands in the fluorescence. Reference 24 gives the value of approximately 35 photons per 100 nm per MeV per event for an FW130 photomultiplier with a corning 7056 glass window. From this the fluorescent response of the tube can be calculated from the geometry and quantum efficiency.

The number of secondary electrons produced is given by (Ref. 24):

$$N_s \approx 0.025 \, \frac{\text{elect}}{\text{MeV/cm}} \left(\frac{dE}{dx}\right)_{si} \qquad (18)$$

$(dE/dx)_{si}$ equals 11.3 MeV/cm. Therefore, equation 18 yields 0.28 electrons. This is small compared to the approximately 100 photoelectrons produced by fluorescence in 7056 glass.

RESULTS

As discussed earlier, two tests were performed. One at the Los Alamos Meson Physics Facility, measured the response of two photomultiplier tubes and an image dissector tube to transient energetic proton beams. The other test, at the Harvard Cyclotron, measured the response these same tubes and assorted silicon photodiodes. Much has been written about the response of similar devices to electrons, gamma-rays and even low-energy protons as shown by the references cited earlier. Very few measurements have been made with high-energy protons. Most of the experimental papers that have been written concerning protons (E>100MeV) use data from spaceborne instrumentation that was an undesirable product of cosmic rays or trapped particles.

LAMPF TEST RESULTS

The test configuration is shown in Figure 3. A summary of the test results are shown in Figures 14, 15 and 16 for the photomultiplier tubes FW129 and FW130 and the image dissector tube F4012, respectively. The tubes were irradiated in two orientations. The first, shown in a, b, and c of Figures 14 15, and 16. The second was with the beam impinging on the side fo the tube so that the protons hit only the glass envelope and first dynodes. The tubes were completely enclosed so that all the response shown in Figures 14, 15, and 16 is due to proton interactions.

Figure 14a shows the response of the FW129 photomultiplier tube to one LAMPF macropulse. The time for the beam to reach 1/e of its maximum value is on the order of 50 µs. This is considerably longer than the tens of nanoseconds response time of the tube. Figure 15b shows this decay in more detail. Figure 14c shows the tube response to the acclerator micropulse. The space between the highest peaks is 4.5 µs or one micropulse. The smaller pulses are after pulsing in the tube. The tube does not completely recover between micropulses.

There are two general types of after pulses discussed in reference 8. The first type is due to light feedback from the anode or dynodes to the cathode. The delay is approximately 50 nanoseconds which is the transit time for the photomultiplier plus the time for the light to return. The second type of after pulse is due to ionization of gas between the cathode and first dynode. According to reference 8 the timing depends on the tube and the gas involved but is usually from 200 ns to over 1 microsecond. The spacing between these pulses is about 800 ns for all three tubes. The shape of the pulses is similar for the FW129 (Figure 14c) and FW130 (Figure 15c) but is slightly different for the F4012 (Figure 16c).

Figures 14d and 15d show the anode response of the FW129 and FW130 by irradiating only the electron multiplier. The response is very similar to irradiating the front of the tube except that it is lower. No measurements were made on the F4012 electron multiplier because of an equipment malfunction.

Figure 15 which shows the resonse of the FW130 is very similar to the FW129 shown in Figure 14 with the exception of the after pulse after the macropulse.

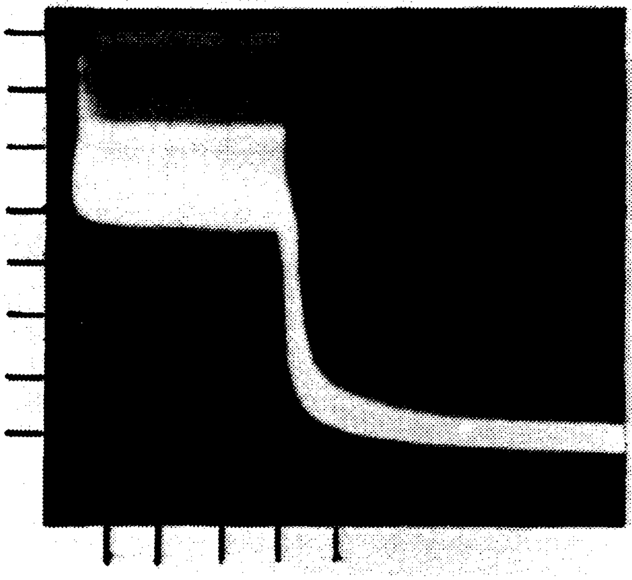

A. Macropulse Structure
1V/DIV
0.2 MS/DIV

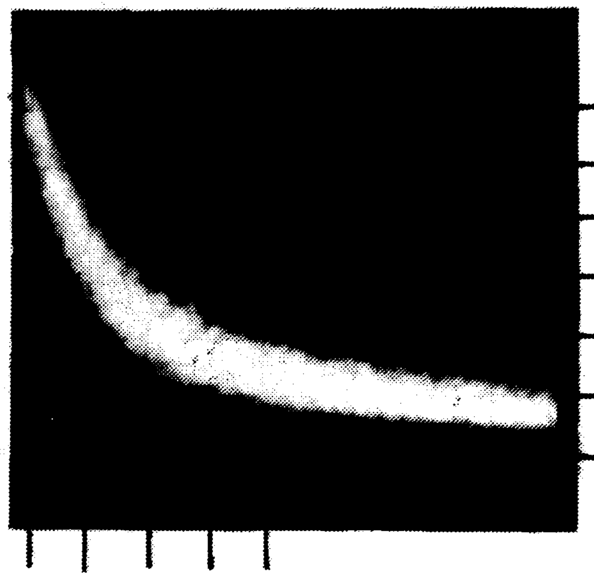

B. Decay
0.5V/DIV
20 μS/DIV

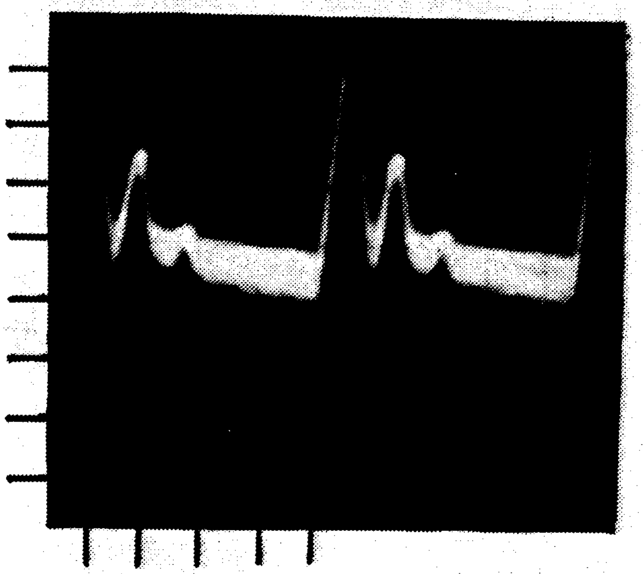

C. Micropulse Structure
1V/DIV
1μS/DIV

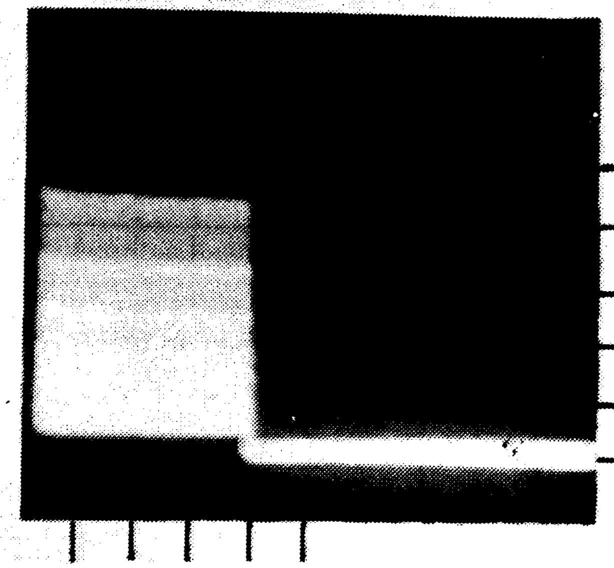

D. Electron Multiplier
1V/DIV
0.2 mS/DIV

Figure 14. FW129 Temporal Response

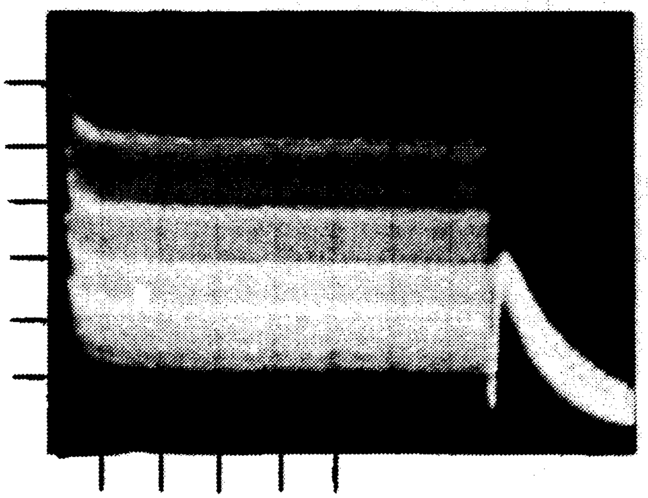

A. Macropulse Structure
1V/DIV
0.1 MS/DIV

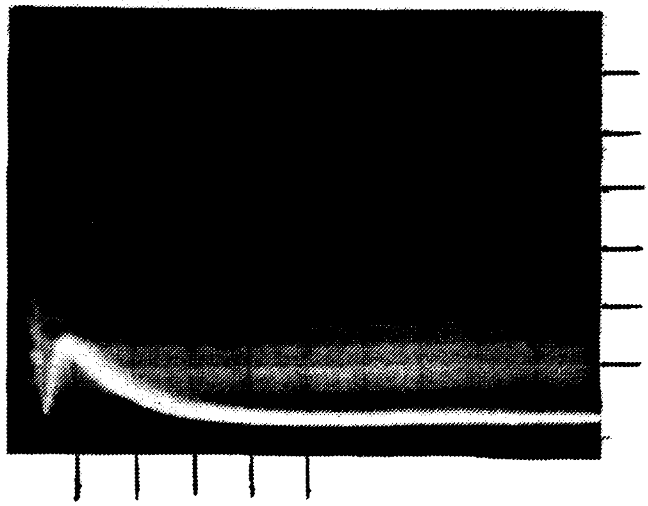

B. Decay
2V/DIV
50 μS/DIV

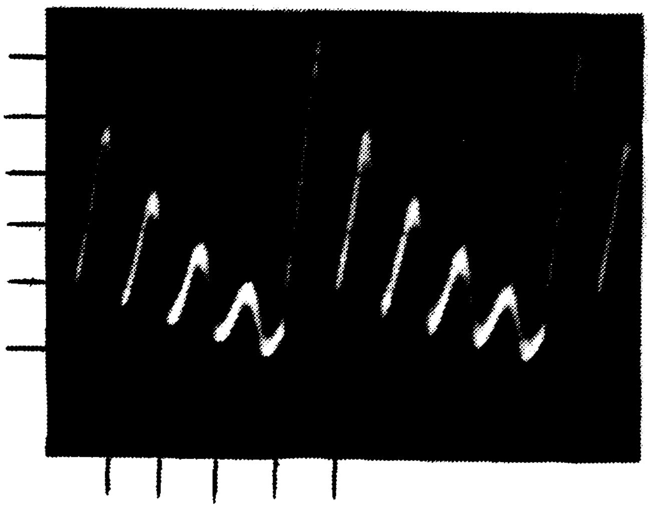

C. Micropulse Structure
0.5V/DIV
0.1μS/DIV

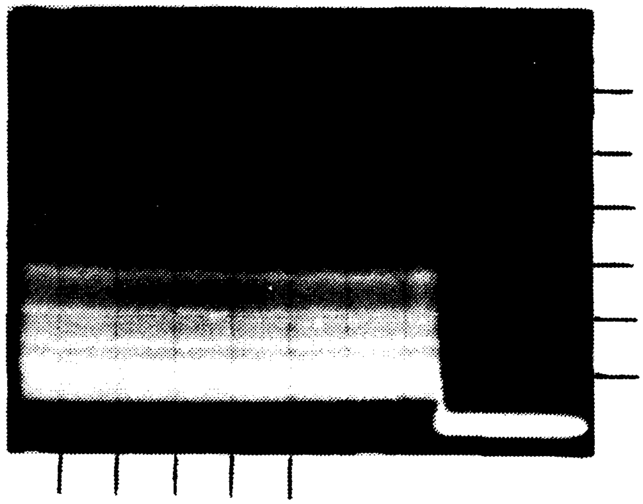

D. Electron Multiplier
1V/DIV
0.1 mS/DIV

Figure 15. FW130 Temporal Response

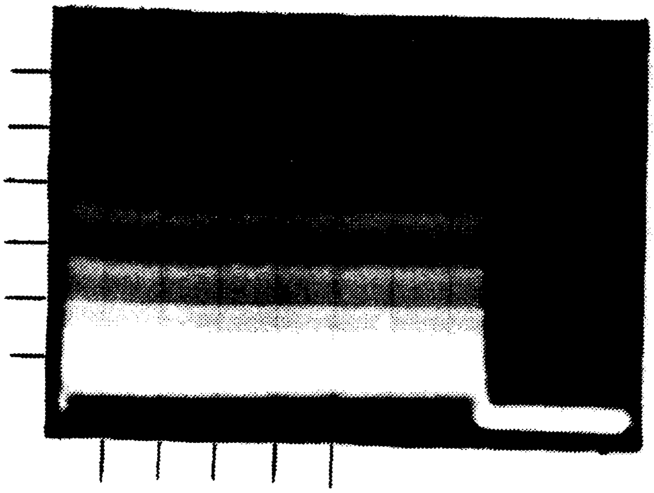

A. Macropulse Structure
0.2V/DIV
0.1 MS/DIV

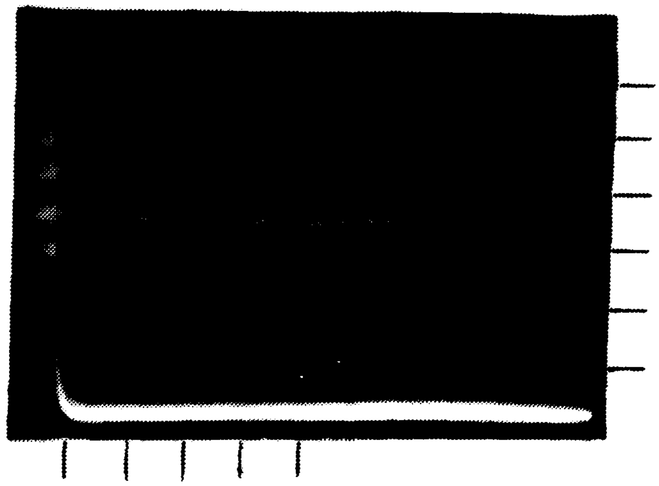

B. Decay
50V/DIV
50 μS/DIV

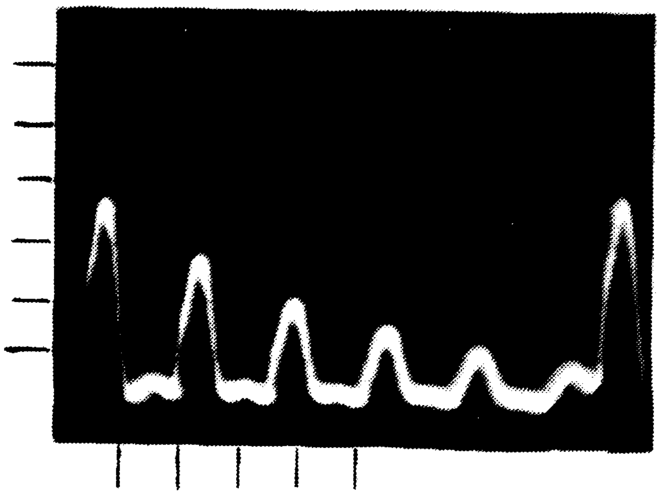

C. Electron Multiplier
0.5V/DIV
0.5 mS/DIV

Figure 16. F4012 Temporal Response

HARVARD CYCLOTRON TEST RESULTS

The two configurations used for the test at the Harvard Cyclotron Laboratory are shown in Figures 3 and 4. In the configuration shown in Figure 3 the device current was measured in one second samples independently of the beam current measurement. At each beam current ten samples of both the beam current and device current were taken. This gave reasonable results when the cyclotron was well behaved and when some effort was made to manually take device and beam readings at the same time (Figures 17, 19, 20, and 21).

In the middle of the test the cyclotron was not as well behaved and the variations in the data were larger than desired. The test configuration was changed to that shown in Figure 4. In that configuration four 10-second samples of both the beam and device currents were taken simultaneously. This resulted in better data statistics, more data points, and better data correlation in about the same time (Figures 22, 23, 24, 25, and 26).

The purpose of these measurements was to determine the response of these sensors to 132 MeV protons. Similar measurements have been made using electrons, gamma-rays, and low-energy protons, but few measurements exist for proton energies in the energy range of particle-beam weapons. In addition, previous measurements have shown that the device current varies linearly with beam current for photomultiplier tubes (Ref. 20 and 25) and for photodiodes (Ref. 26, 27, and 28). An effort was made during these measurements to determine the slope of the device current as the beam current was varied.

Figures 17 and 19-26 show the response of the multiplier phototubes and photo diodes to changes in the cyclotron beam current. The abscissa is the beam current and the ordinate is the anode current with the dark current subtracted. The error bars represent the standard deviation of the 10 samples of beam current and device current that constitute each data point. The line is determined by least squares fit of the data. The horizontal line labeled dark current in Figures 19, 21, 22, 23, 24, 25, and 26 is the dark current of the device measured at the beginning of each test. Dark current was measured for the other devices but was too low to be shown on the graph.

The line below the measured data points represented by filled circles in Figures 22, 23, 24, 25, and 26 is the measured radiation induced dark current which appeared in the photodiodes and lasted for at least hours after the measurements. This dark current was probably a leakage current which is proportional to the number of recombination centers in the space charge region (Ref. 2).

The other line represented by the points in Figures 17, 19, 20, 21, 22, and 23 is a least square fit of the calculated radiation induced dark current. Each point is calculated from an extrapolation of the samples that make up a data point to zero beam current. What remains is the radiation induced dark current. Only those points taken while the cyclotron was well behaved are included.

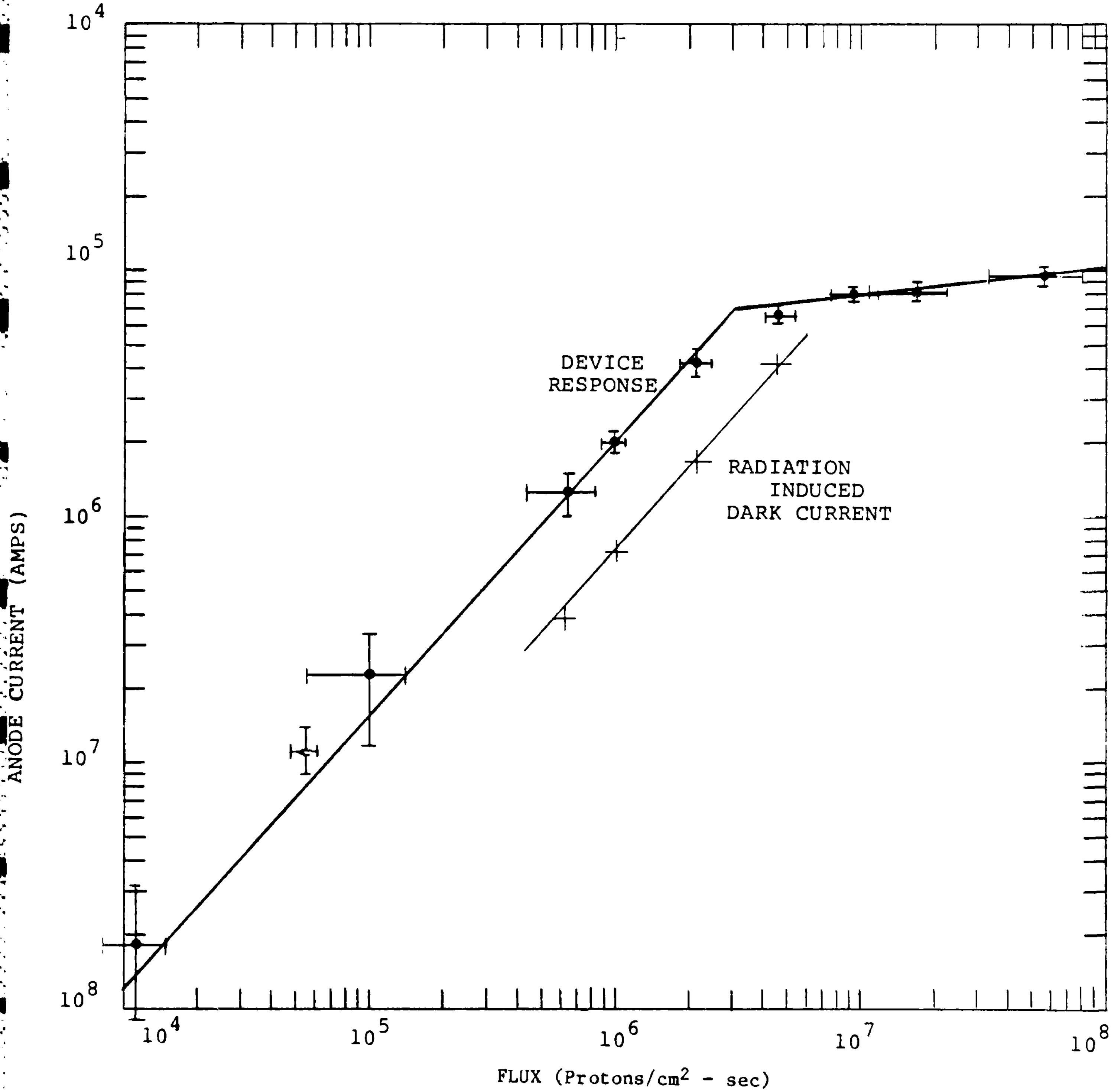

Figure 17. FW 129 Multiplier Phototube Response

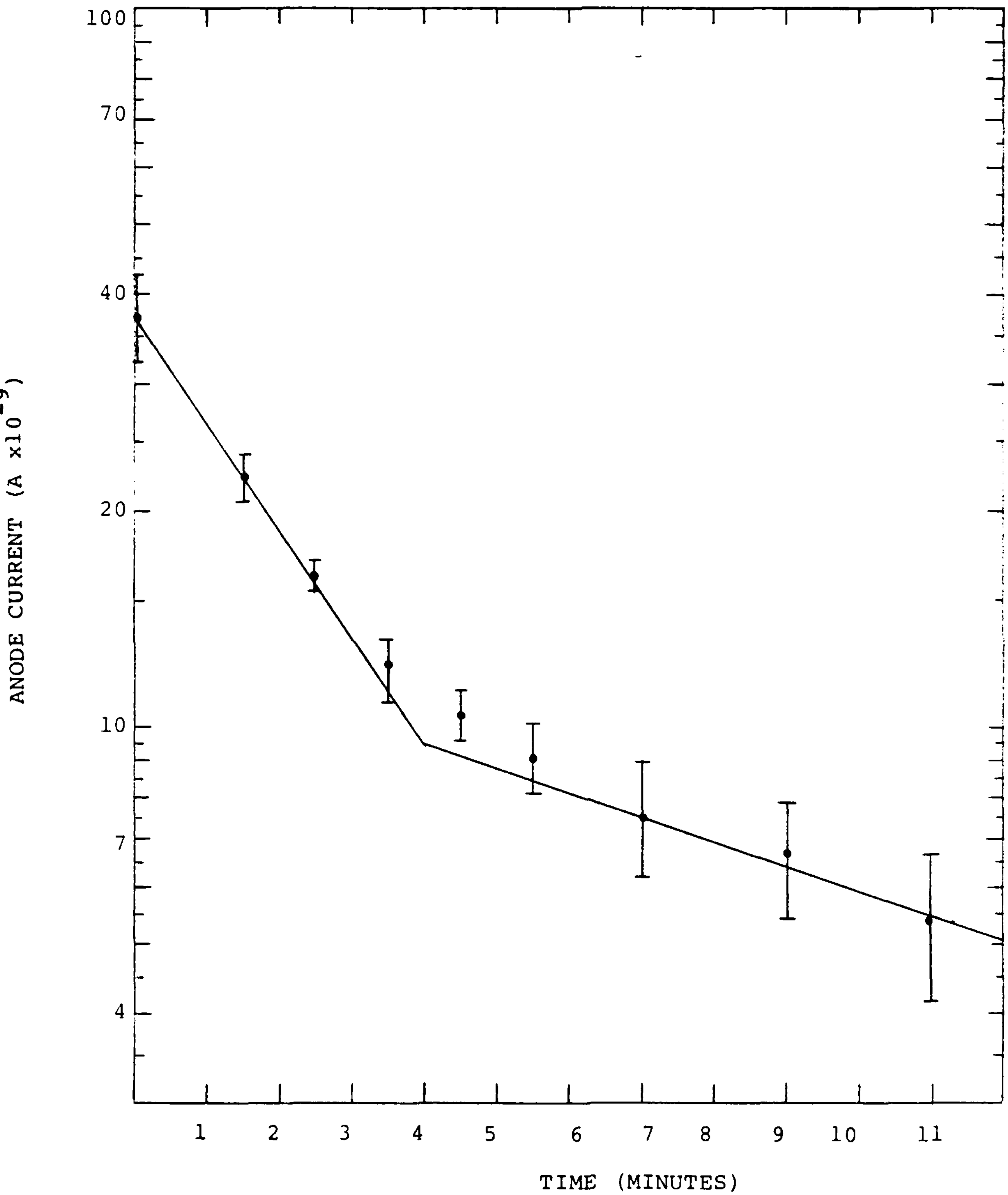

Figure 18. FW 129 Temporal Response

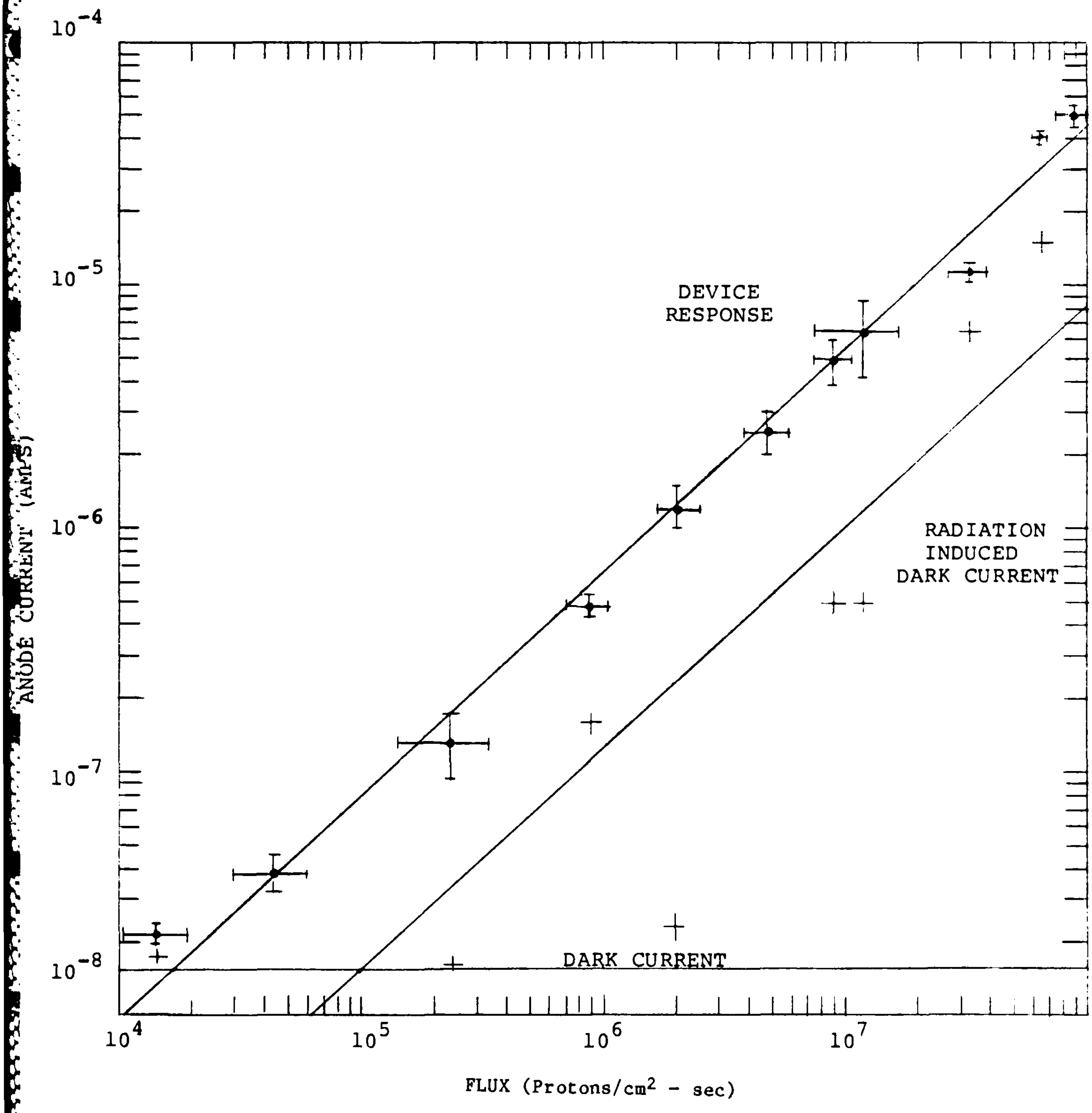

Figure 19. FW130 Multiplier Phototube Response

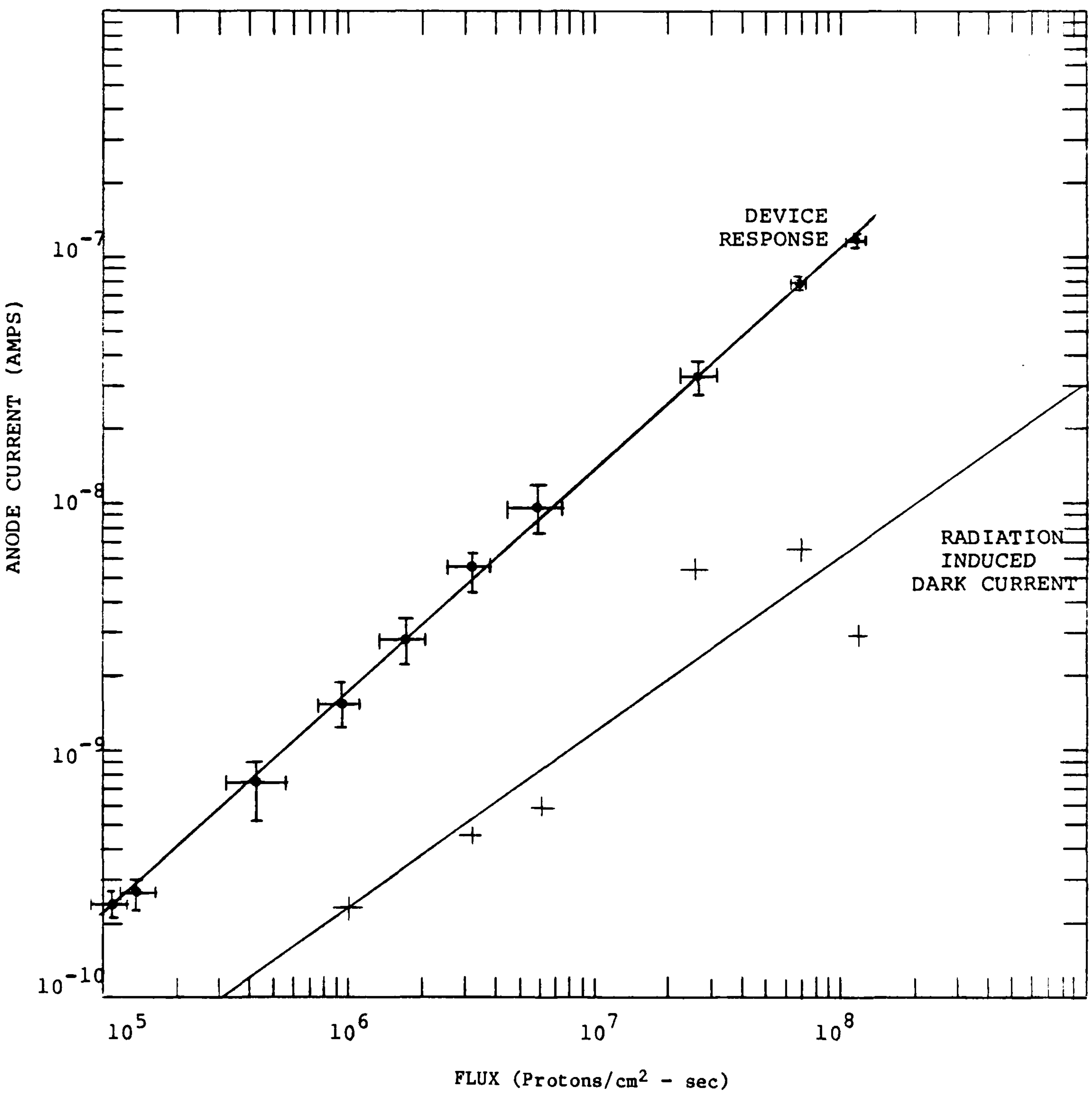

Figure 20. 4012 Multiplier Phototube Response

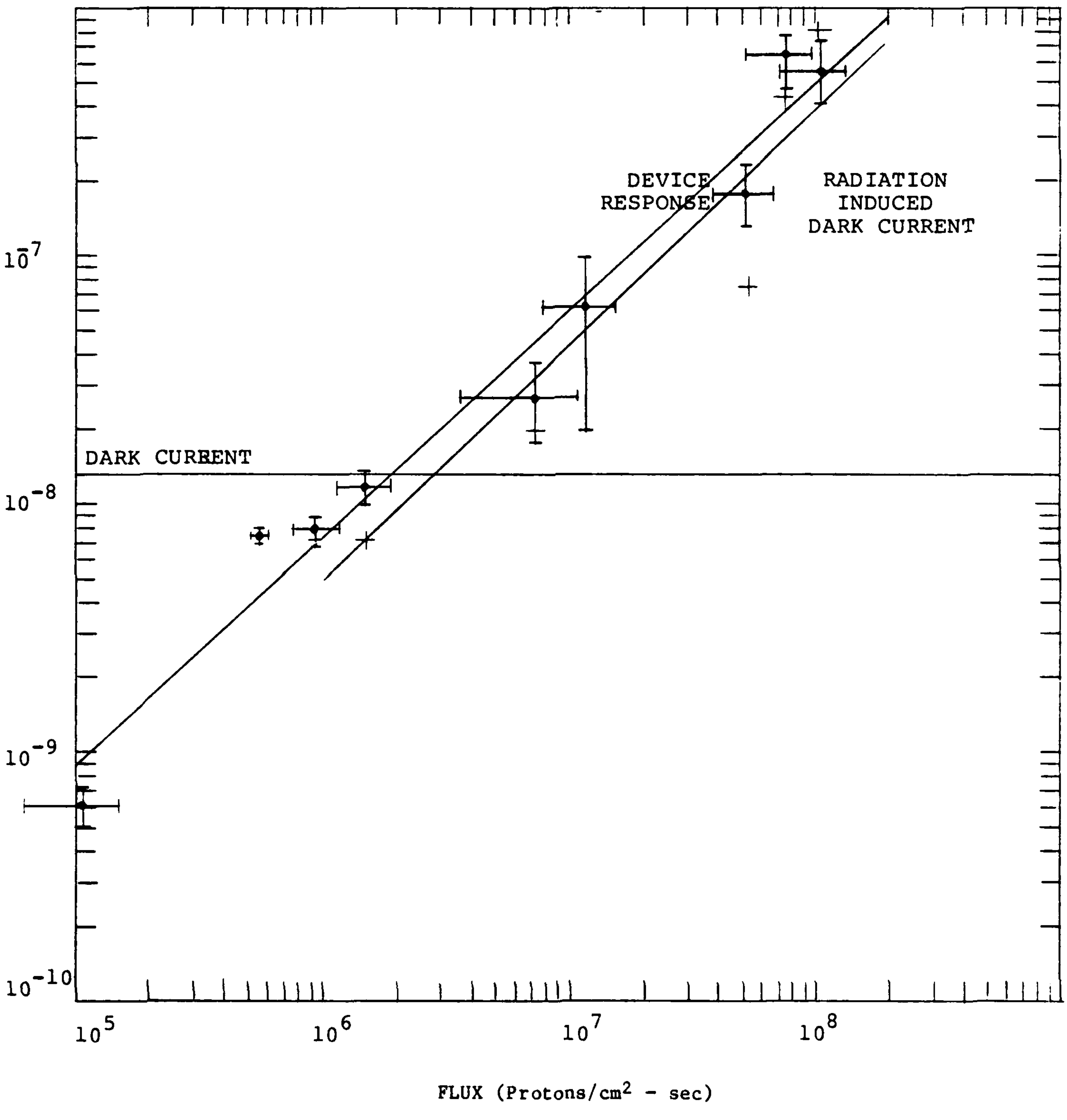

Figure 21. 30902E Avalanche Photodiode Response

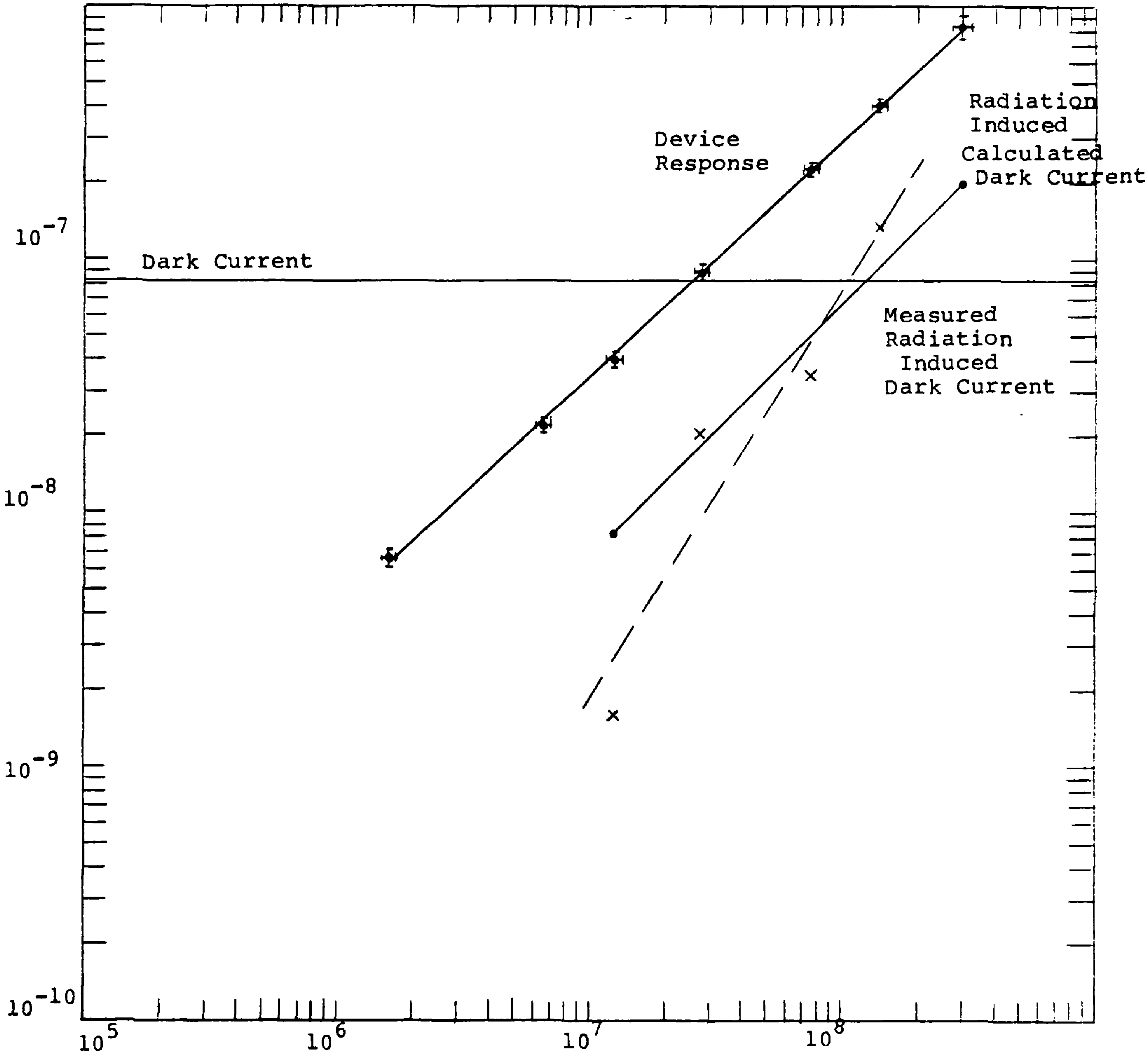

FLUX (Protons/cm^2 - sec)

Figure 22. 30916E Avalanche Photodiode Response

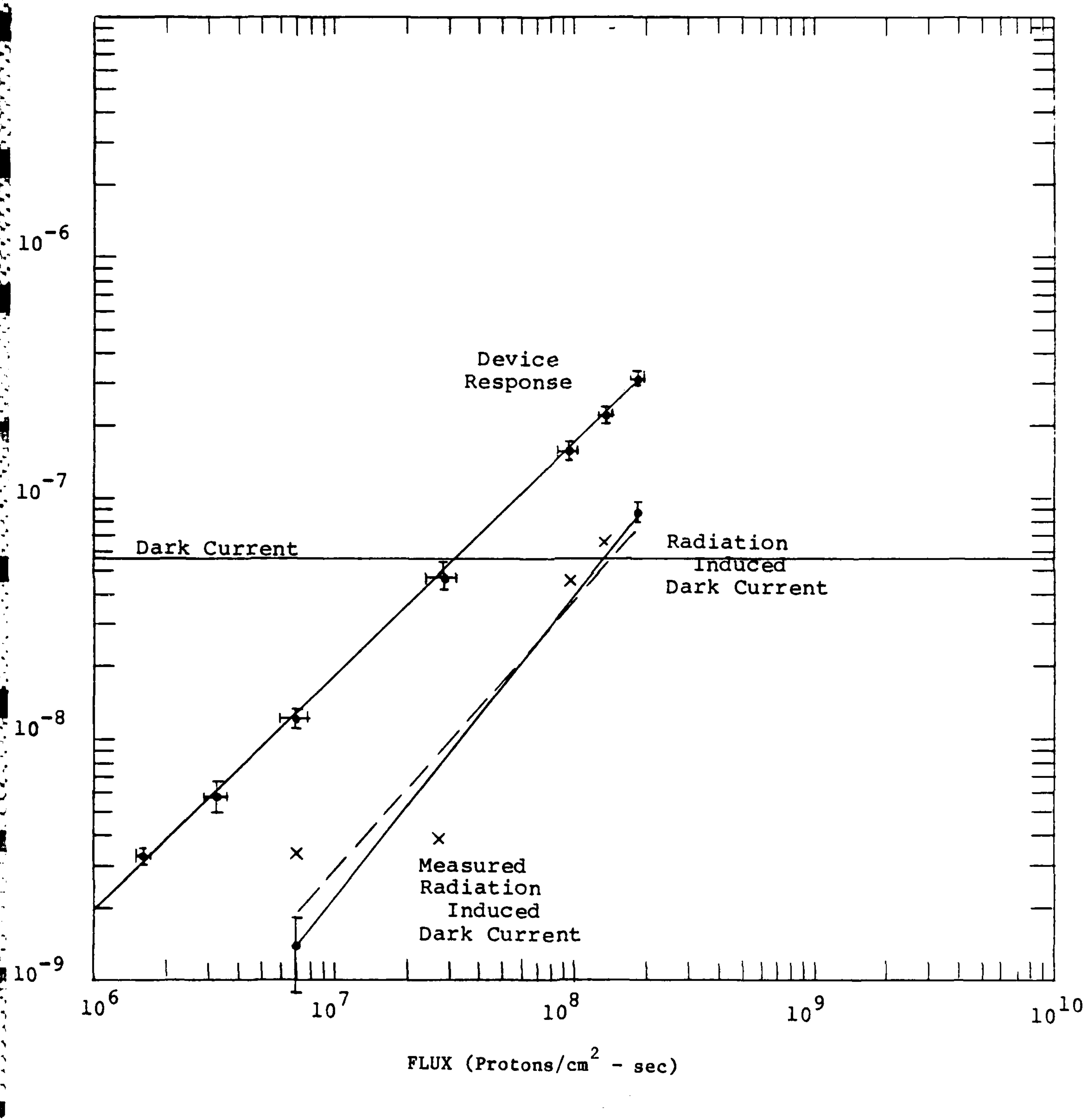

Figure 23. 30817E Avalanche Photodiode Response

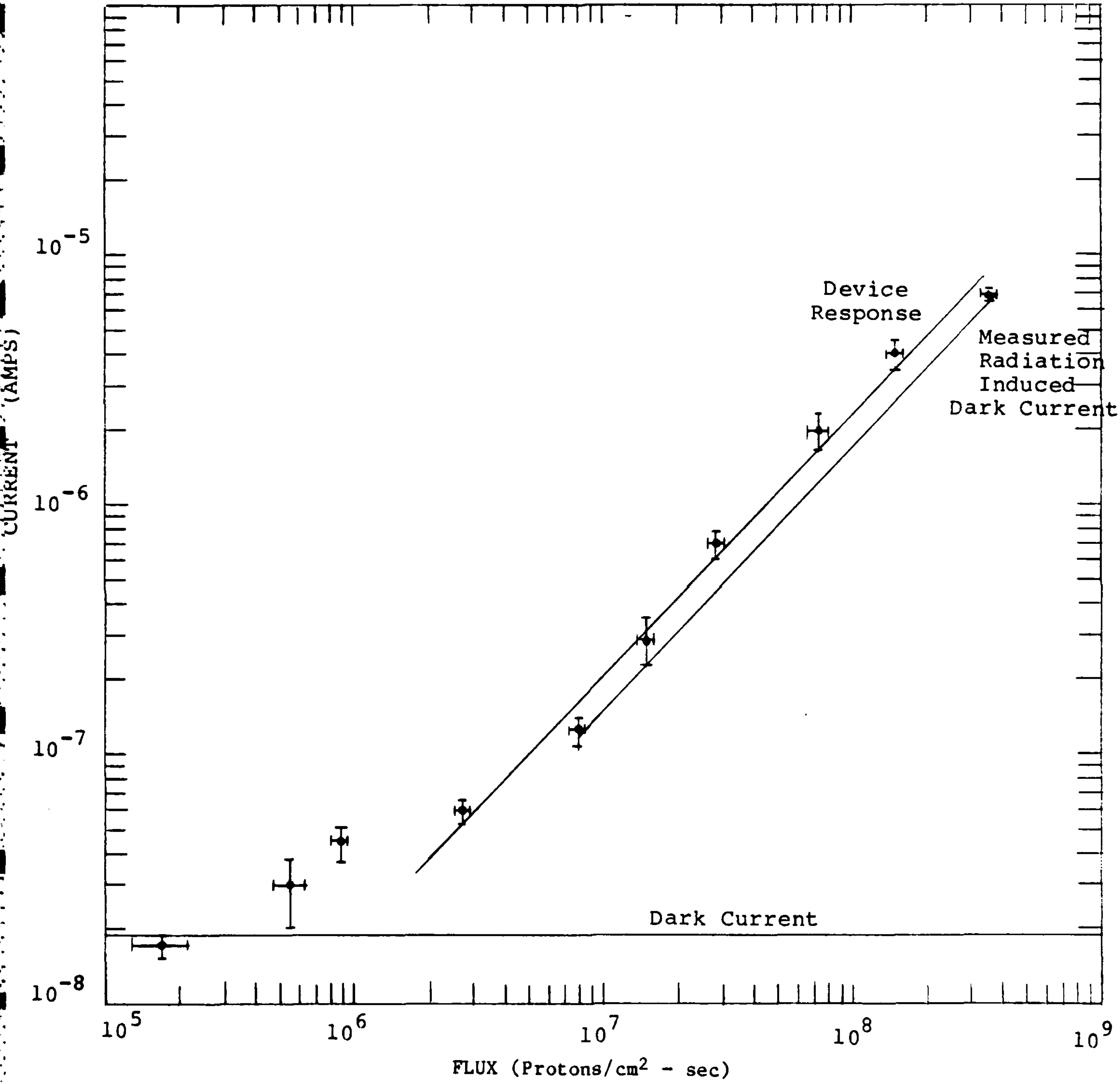

Figure 24. SD-100-12-22-021 Photodiode Response

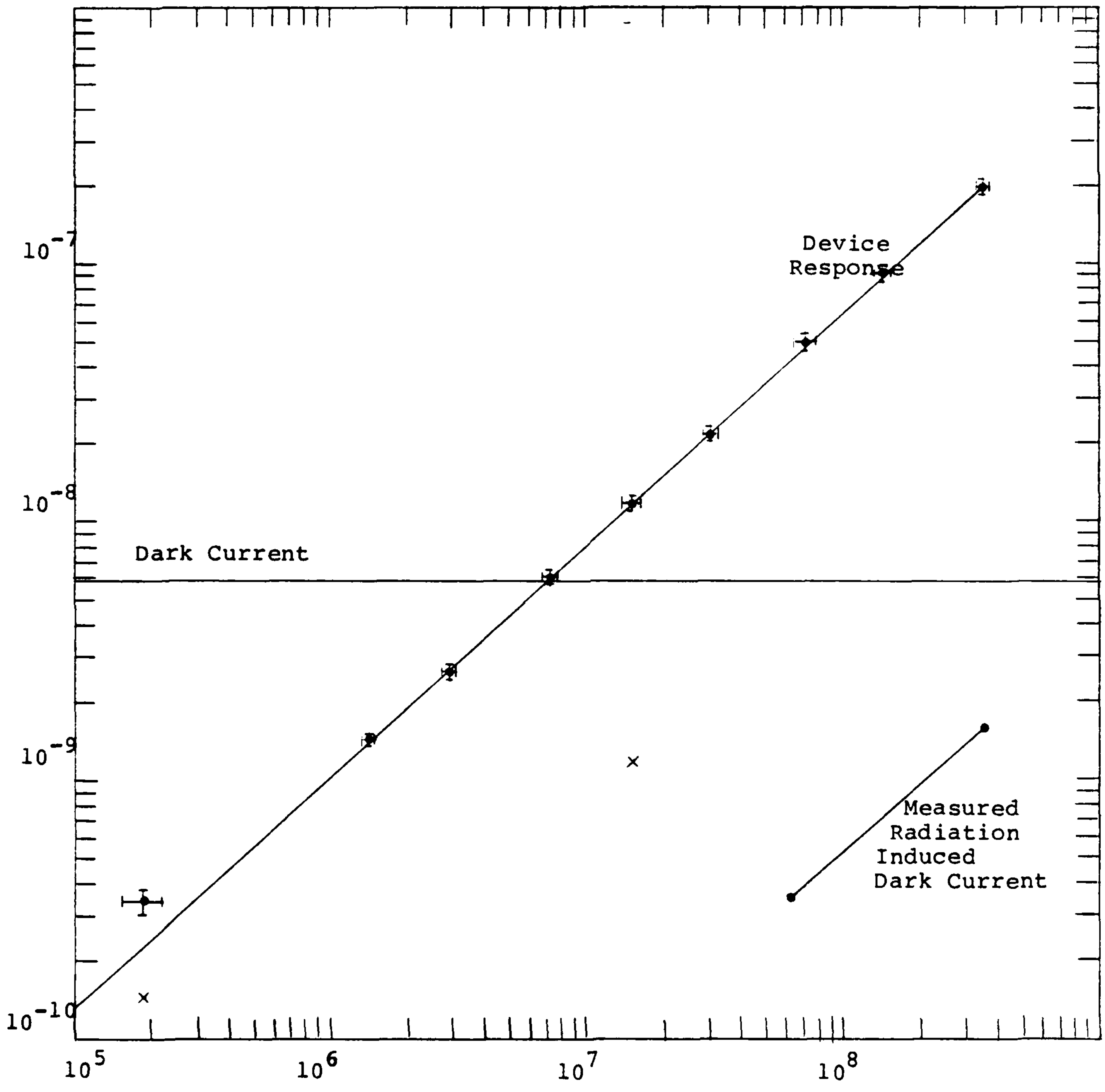

Figure 25. SD-100-12-12-021 Photodiode Response

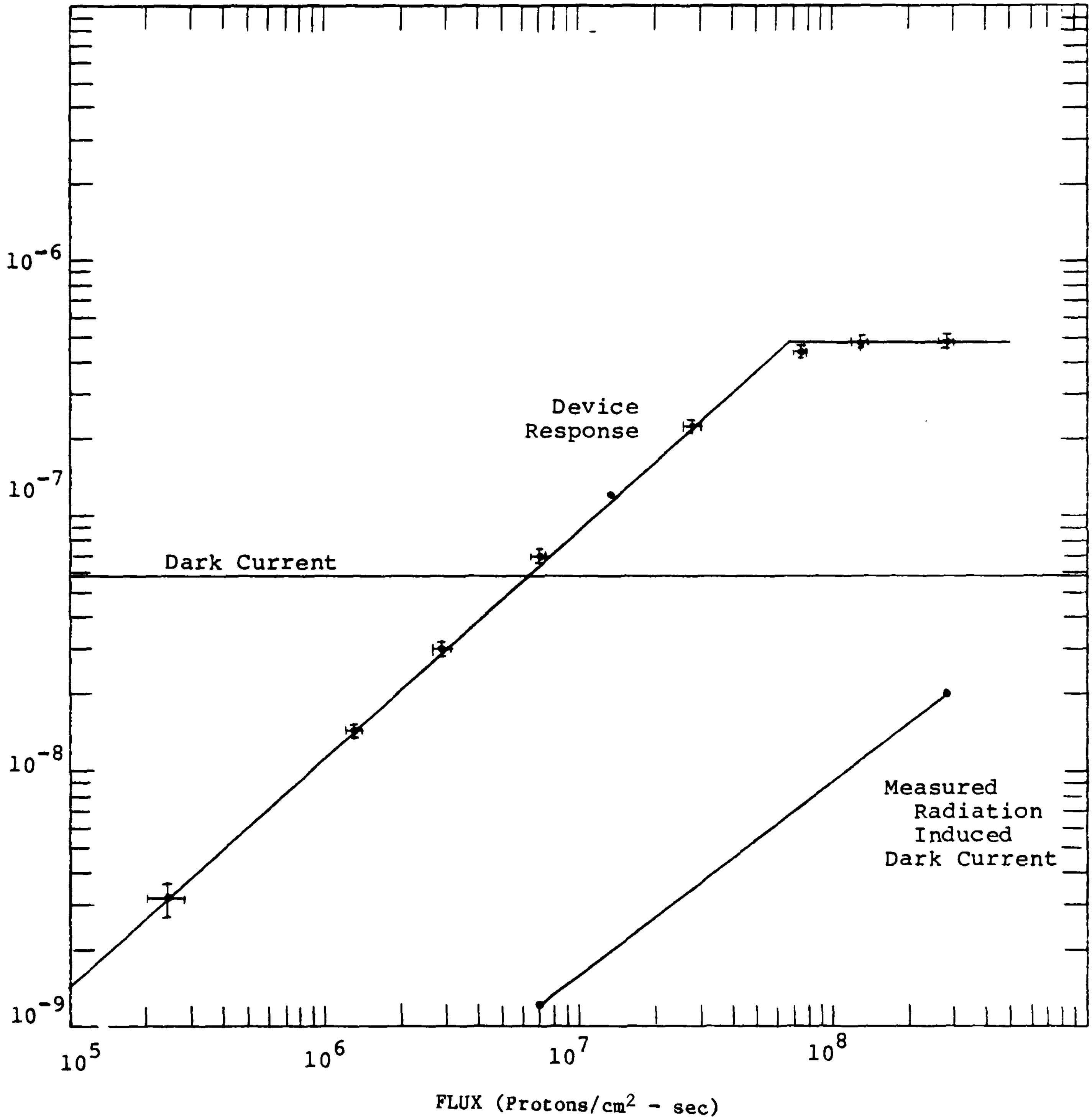

Figure 26. PIN-10 Photodiode Response

A significant difference between the multiplier phototubes and the photodiodes was observed. The radiation induced dark current for the tubes decayed in a few minutes while, as noted above, the photodiode radiation induced dark current continued for hours. Figure 18 shows the anode current of the FW129 tube as a function of time. There appears to be two components of this decay. These data were fitted to a curve of the form:

$$I_A = I_1 \exp(-t/\tau_1) + I_2 \exp(-t/\tau_2)$$

One component has a time constant of approximately 3.2 minutes and the other of 12.2 minutes. Other components, both longer and shorter, may also be present. These are probably due to long term phosphorescence in the faceplate and glass envelope caused by trapping of electrons and holes at lattice defects and their release by thermal agitation (Ref. 24).

The data in Figures 17 and 19-26 were plotted on a log-log scale and fitted from equation of the form:

$$I_A = aI_B^{\,b} + I_D$$

where I_A is the anode current, I_B is the beam current, I_D is the dark current and a and b are constants. Table 7 lists the slope b for each device tested.

Table 7. Slope and Arr

DEVICE	SLOPE	CORRELATION	Arr(rad/Phot)
Photomultipliers			
FW129	1.07	0.980	1.48×10^{-9}
FW130	0.908	0.988	1.99×10^{-8}
F4012	0.905	0.999	4.07×10^{-8}
Photodiodes			
30902E	0.909	0.983	2.06×10^{-10}
30916E	0.933	0.999	2.52×10^{-10}
30817E	0.966	0.999	4.76×10^{-10}
SD-100-12-22-021	1.05	0.995	4.87×10^{-13}
SD-100-12-12-021	0.859	0.999	9.98×10^{-12}
PIN 10	0.902	0.998	6.25×10^{-13}

Of the detectors tested only the FW129 photomultiplier and the SD-100-12-22-021 had slopes equal to or greater than one.

The sensitivity of the detectors to ionizing radiation is not very well described by the current out of the device for a certain dose rate because of differences of geometry and material type. Reference 26 defines a detector figure of merit Arr that can be used to compare detectors in an ionizing radiation environment. Arr is defined by the optical current density per unit optical flux divided by the radiation induced current density per unit dose rate.

$$Arr = (Jopt/\phi)\ (\dot{\gamma}/Jrad) \qquad (19)$$

where Jopt is the optical current density; ϕ is the incident optical flux; $\dot{\gamma}$ is the dose rate in rads (si) and Jrad is the radiation induced current density. The conversion factor from particle flux in proton/cm^2 sec to rads/sec is 7.75×10^{-8} rads-cm^2 per 132 MeV proton. The higher Arr the less sensitive the device is to ionizing radiation. Arr shows that the device with the highest output current per ionizing radiation flux of those tested, the FW129, is actually one of the least radiation sensitive and the device with the lowest output current per ionizing radiation flux, the SD-100-12-12-021, is one of the most radiation sensitive.

It is interesting to note that the photomultiplier tube are a group of the most radiation resistant followed by the avalanche photodiodes and then the other photodiodes. This combined with the fast response, great sensitivity, large area, and rapid recovery mean photomultipliers are advantageous to use in a radiation environment.

The FW129 photomultiplier tube and the PIN 10 photodiode show saturation effects. Nonlinear effects in photomultiplier tubes are caused either by space charge limiting, cathode resistivity, focusing, change of collection efficiency or excess signal current (Ref. 18). Space charge only becomes a problem for currents in the milliampere range. Cathode resistivity is a problem in tubes with a semitransparent S-11 cathode. This is demonstrated by the 30 mW maximum anode power specification for the FW129 and shown in reference 8. The S-20 photocathode in the FW130 has order of magnitude lower resistivity (reference 8). This nonlinearity could have been avoided for these currents by using a different resistive divider, but does show a significant radiation effect.

SYSTEM CONSIDERATIONS

In this section the effects of radiation will be considered on two typical systems. One system will be modeled after the INSAT very high resolution imaging radiometer (IVHRR) designed and built by ITT-A/OD. This is an imaging system with a 20.3 cm diameter telescope on a stabilized spacecraft in geosynchronous orbit. The detector current is given by:

$$I_A = \phi_S R \qquad (20)$$

where ϕ_S is the scene energy and R is the detector responsivity. The scene energy can be found from the area of the aperture, the solar specral irradiance, the optical transmission, the albedo and the field of view by:

$$\phi_S = \frac{(\pi D_a^2)}{4} I_S \tau\rho\theta^2 \qquad (21)$$

where I_S is the solar spectral irradiance; D_a is the aperature diameter; τ is the optical transmission; ρ is the albedo and θ is the field of view. Typical values for the IVHRR are:

$\tau = 0.29$ for the optical train and filters
$\rho = 0.025$
$R = 0.5$ A/W
$I_S = 1.04 \times 10^{-2}$ W/cm²/str
$\theta = 7.7 \times 10^{-5}$ rad

For this case ϕ_S is 1.45×10^{-10} watts and the detector current is 7.25×10^{-11} A. If this is put into the amplifier shown in Figure 27 with a feedback resistor of 1.5×10^7 ohms, the signal level is approximately 1.4×10^{-3} volts.

Various terms constitute the noise of the system. The main contributors are the dark current shot noise, detector Johnson noise, 1/f noise, gate leakage shot noise, feedback Johnson noise and amplifier voltage noise. The equations and values for these noise voltages for the IVHRR are given in Tables 8 and 9. The signal-to-noise ratio is 60 to 1 for a bandwidth of 2272 Hz. The bandwidth is found by taking one-half of the elemental dwell time.

The noise from the radiation induced current is shot noise equation given by:

$$i_{rr}^2 = 2eI_r \qquad (22)$$

where i_{rr} is the radiation induced noise current density and I_r is the radiation induced current.

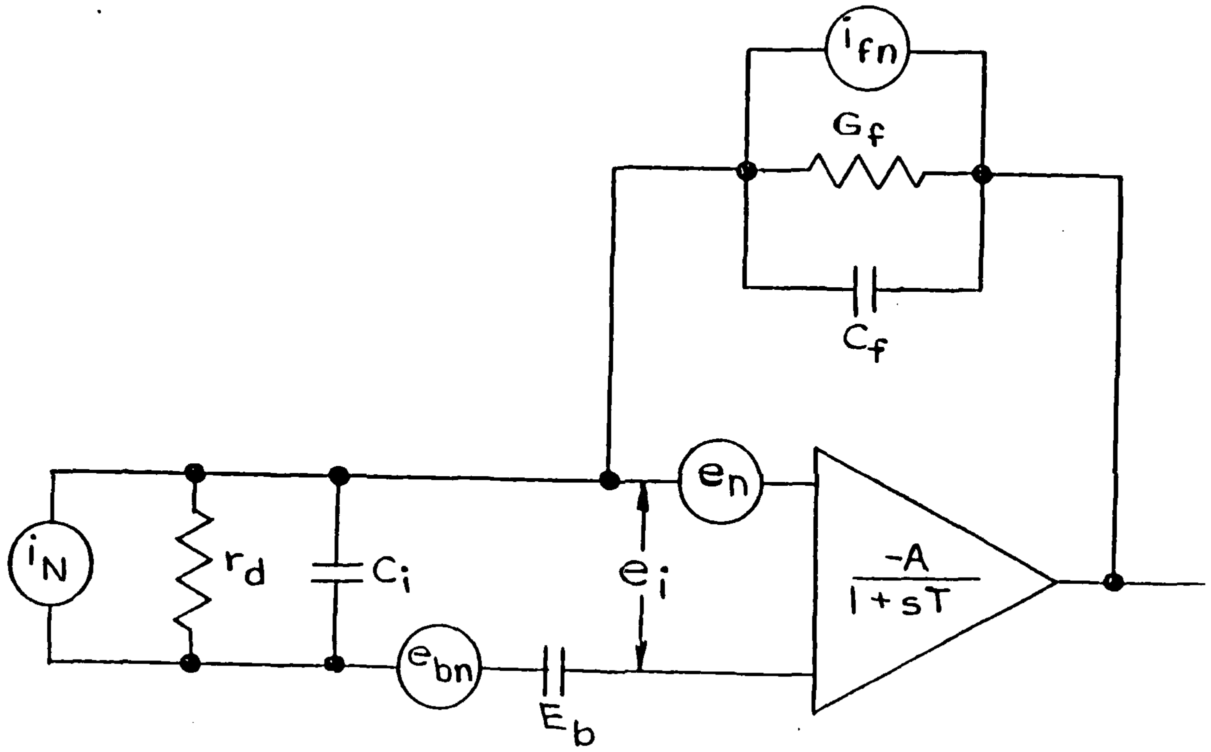

Figure 27. Equivalent Noise Circuit

Table 8. Visible Channel Noise Sources

Dark Current Shot Noise, i_{ds}

$$i_{ds}^2 = 2eI_{dc}$$

where I_{dc} = detector dark current and i_{ds} is the shot noise spectral density.

Detector Johnson Noise, i_{dj}

$$i_{dj}^2 = 4KT/R_d$$

where K = Boltzmann's const,
T = temperature, and
R_d = detector resistance

1/f Noise, $i_{1/f}$

$$i_{1/f}^2 = i_{ds}\ f_k^{\beta}/f^{\beta}$$

where f_k is knee frequency
β = slope of 1/f noise

Gate Leakage Short Noise, $i_{g\ell}$

$$i_{g\ell}^2 = 2eI_{g\ell}$$

where $I_{g\ell}$ = FET gate leakage current

Feedback Johnson Noise, i_{fn}

$$i_{fn}^2 = 4KT/R_f$$

where R_f = feedback resistance

Amplified Voltage Noise, e_n

$e_n^2 = (20\times10^{-9})^2\ (1+f_k/f)$ for the OP15 operational amplifier

Signal Shot Noise, iss

$$i_{ss}^2 = 2ei_s = 2e\phi_s R$$

Table 9. Nominal Noise Voltages at Room Temperature

$I_{dc} = 5.0 \times 10^{-10}$ A
$\beta = 1.0$
$f_k = 1$ Hz
$I_{g\ell} = 20$ PA
$\Delta f = 2272$ Hz

Noise Source	Value
Detector Shot Noise	9.0×10^{-6} V
Detector Johnson Noise	4.1×10^{-6} V
1/f Noise	6.0×10^{-7} V
Gate Leakage Shot Noise	1.8×10^{-6} V
Feedback Johnson Noise	1.4×10^{-5} V
Amplifier Voltage Noise	1.7×10^{-6} V
Signal Shot Noise	4.0×10^{-6} V
RSS SUM	1.8×10^{-5} V

For a signal-to-noise ratio of one the RSS noise voltage must equal the signal current. For the parameters chosen the radiation current would be 1.7×10^{-5}A for a signal-to-noise ratio of 1. Typically a signal-to-noise ratio of 5.5 to 1 is required for 99% reliability and 10^{-3} false alarm rate. In that case the radiation induced current could not exceed 5.5×10^{-7}A. For other systems the answer would be somewhat different but the method would be the same.

The second system to be considered contains an image dissector tube such as the F4012 used in a tracking mode. The field of view of the scan platform is assumed to be 20° x 20°; the camera field of view 5° x 5° and the 200 μm image dissector aperture field of view 0.1° x 0.1°. Using a 115 mm focal length f/2 lens, the collecting area is $2.6 \times 10^{-3} m^2$. A star of magnitude +2 has an illuminance of 4×10^{-7} lumens/m^2. The flux onto the cathode is then 1×10^{-9} lumen. The typical cathode luminous sensitivity is 100 μA/lumen. The current from the photocathode is 1.0×10^{-13}A. The anode current is 1.0×10^{-7}A for a gain of 1×10^6 from the electron multiplier.

The radiation noise current spectral density at the aperture is given by equation 22 modified by the gain G (Ref. 29).

$$i_{rr}^2 = 2e\ (I_r/G) \qquad (23)$$

where I_r is the radiation induced output of the device. To find the noise at the output i_{rr}^2 is multiplied by the gain G squared and an experimentally determined noise factor k. The output noise spectral density is then given by:

$$i_{nr}^2 = 2ekGI_r \qquad (24)$$

The total noise is found by adding the signal shot noise to the radiation shot noise.

$$i_n^2 = 2ekG\ (I_r + I_A) \qquad (25)$$

For the F4012 the noise factor is a maximum of 4. The noise current is found by multiplying the square root of equation 25 by the bandwidth Δf.

A threshold decision maker requires a signal-to-noise ratio of 5.5 for 99% reliability and 10^{-3} false alarm rate. From the output signal current for a +2 magnitude star and the noise current the radiation induced output current for a signal-to-noise ratio of 5.5 is found to be 1.4×10^{-8} amps for the bandwidth of the example above (2272 Hz). The noise current is the RSS sum of the radiation current induced noise current and the signal shot noise current. The other noise sources such as dark current shot noise and Johnson noise are assumed to be small. A radiation induced current greater than 1.4×10^{-8} amps will reduce the signal-to-noise ratio below 5.5 for an object as bright as a star of magnitude +2 and begin to affect the ability to track the object. The radiation induced current can be converted to radiation flux using the measured curves Figures 17, 19, and 20. Table 10 summarizes these results for stars of various magnitudes (or objects of the same brightness). The lines in the last column indicate the S/N exceeds 5.5 for this system viewing an object of this magnitude without additional radiation induced noise.

Table 10. Star Tracker Current to Achieve a Signal-to-Noise Ratio of 5.5

STAR MAGNITUDE, ϕ	ILLUMINANCE	PHOTOCURRENT	ANODE CURRENT (10^6 GAIN)	MAX. RADIATION CURRENT FOR S/N OF 5.5
-1	3.2×10^{-6} lm/m	8×10^{-13}A	8×10^{-7}A	6.5×10^{-6}A
0	1.6×10^{-6} lm/m	4×10^{-13}A	4×10^{-7}A	1.4×10^{-6}A
+1	8×10^{-7} lm/m	2×10^{-13}A	2×10^{-7}A	2.6×10^{-7}A
+2	4×10^{-7} lm/m	1×10^{-13}A	1×10^{-7}A	1.4×10^{-8}A
+3	2×10^{-7} lm/m	5×10^{-14}A	5×10^{-8}A	--
+4	1×10^{-7} lm/m	2.5×10^{-14}A	2.5×10^{-8}A	--

Another approach is to calculate the time required to acquire a signal assuming a signal-to-noise ratio of 5.5. The acquisition time per pixel is approximately equal to:

$$\Delta t = 1/2\ \Delta f \tag{26}$$

where Δf is the bandwidth. This can be substituted into equation 25 and Δt calculated from:

$$\Delta t = \frac{(S/N)^2\ ekG\ (I_r + I_A)}{I_A^2} \tag{27}$$

For $I_r=1.0\times10^{-7}$A, S/N=5.5, k=4, $G=1\times10^6$ and $I_A=1\times10^{-7}$(M=+2), Δt equals 1.9×10^{-4}S. According to reference 20 an image dissector can jump between adjacent pixels as fast as 1 μs and across a full image diameter in 100 μs depending on the external deflection circuits. To cover the whole 20° x 20° field of view with 50 percent overlap requires 1.6×10^5 pixels. The total time for acquisition is 34 seconds. These results are summarized in Figure 28 for stars of magnitude -1 to +6 and radiation induced currents of 10^{-9} to 10^{-5}A. Once the object has been acquired the scanning pattern can be changed to more efficiently cover the area.

Still another method is to choose an acceptable time to complete a scan of the total field of view using a desired system. The properties of the optical system and the sensor will determine the dwell time. Then the signal-to-noise can be calculated from equation 27. Other supporting systems such as a rapid acquisition system will allow a smaller area to be searched. Figure 29 shows the signal-to-noise as a function of the radiation induced current at the anode for the system discussed above and a total scan time of 1 minute for a 20° x 20° field (3.75×10^{-4} seconds/pixel). The horizontal line is a signal-to-noise of 5.5.

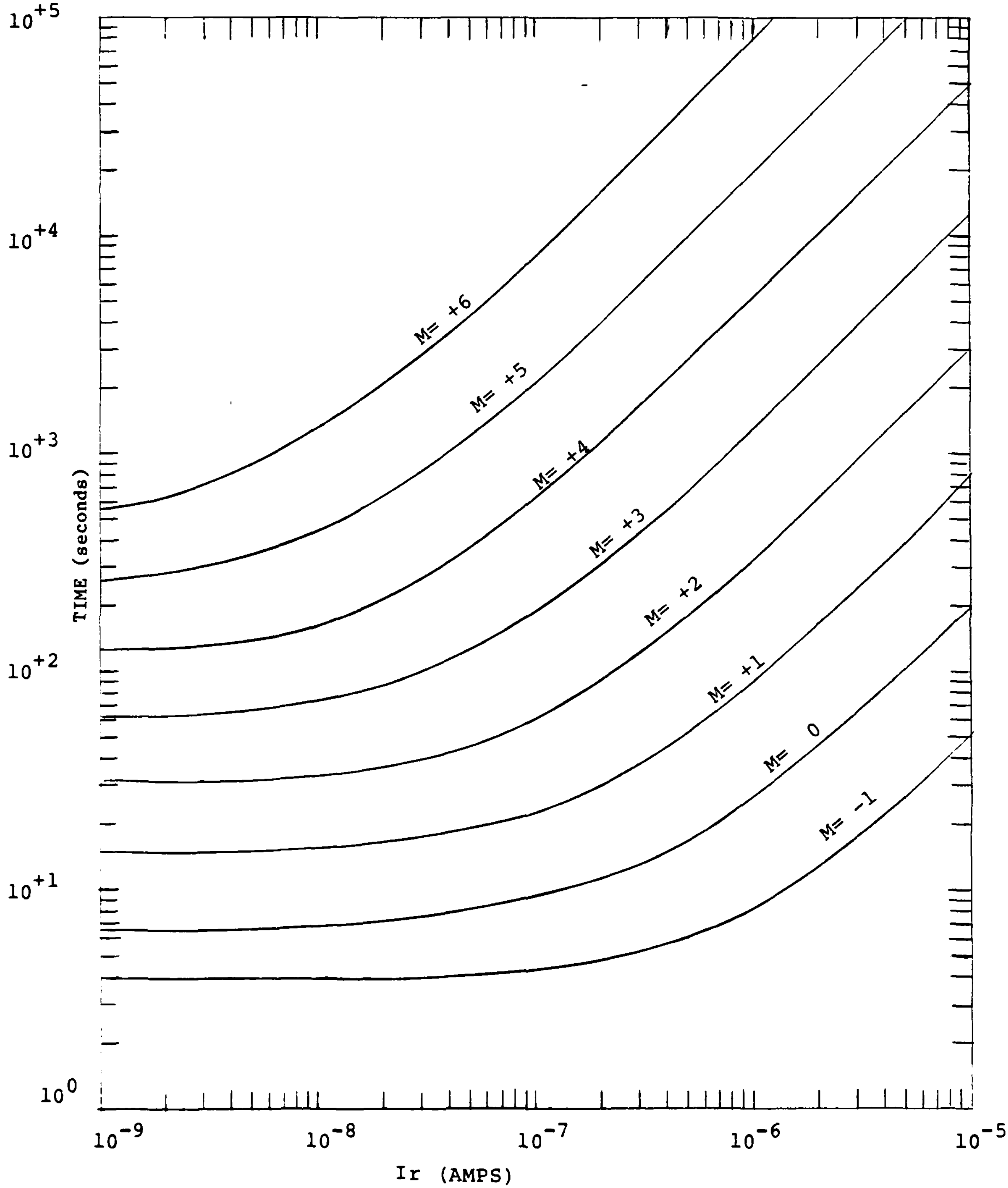

Figure 28. Tracker Acquisition Time

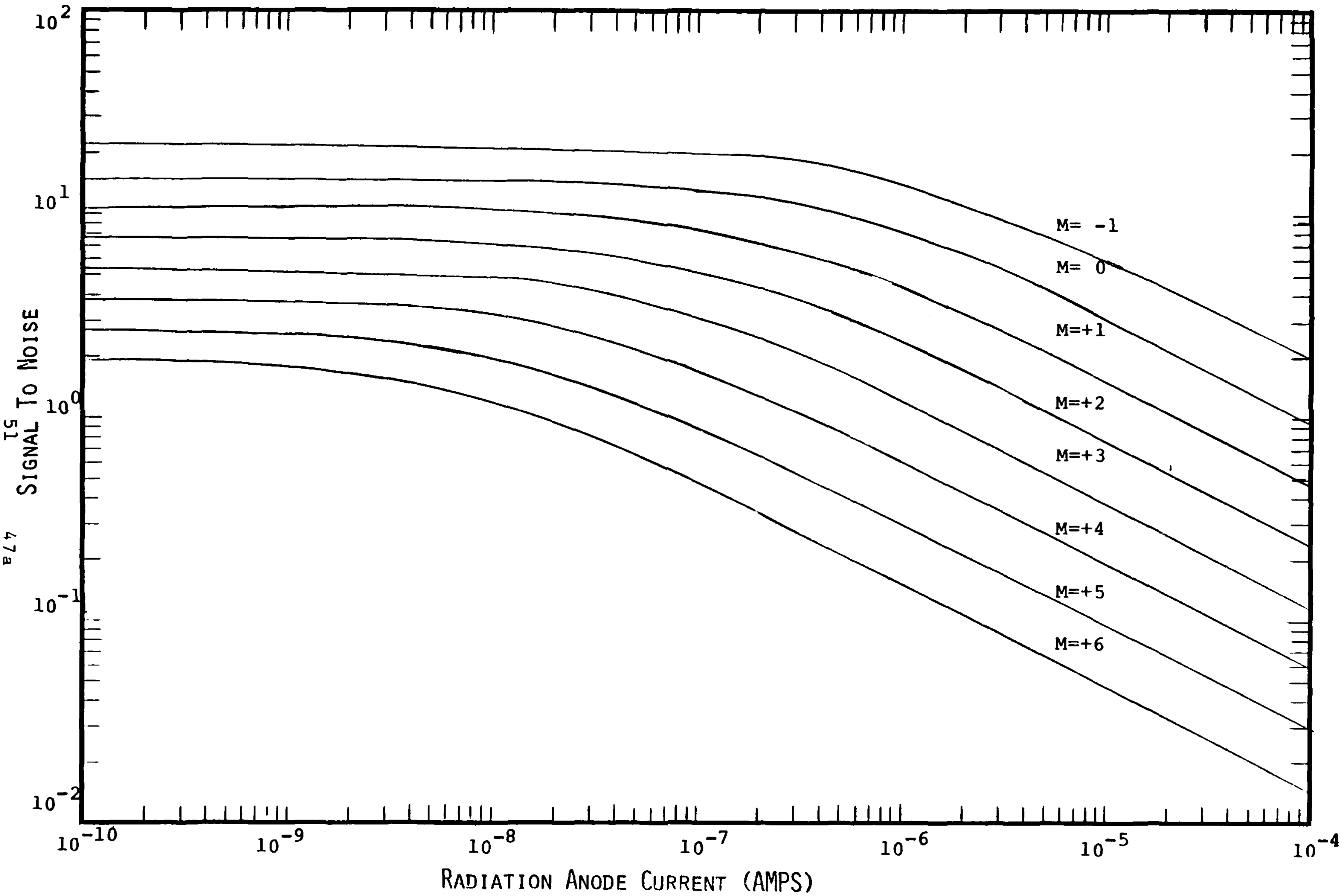

Figure 29. Tracker Signal-to-Noise

SUMMARY

This report has presented the results of an experimental study of the interaction of protons with energies in the hundreds of MeV range with selected electro-optical sensors. Two tests were performed: one at the Los Alamos Meson Physics Facility to measure the temporal response of multiplier phototubes and the other at the Harvard Cycletron Laboratory to measure the transient response of photomultiplier tubes and silicon photodiodes These tests were a preliminary survey of frequently studied devices to serve as a comparison with gamma ray, electron, and low-energy proton measurements.

A simple model of each device was prepared and the expected radiation effects described. These were checked against the measurements and found to be in reasonable agreement. More detailed models need to be prepared.

The results of the test of photomultiplier tubes at the Los Alamos Meson Physics Facility show that most of the response comes from the front of the tube (faceplate and photocathode). Long term effects are present for microseconds after the beam is switched off. In addition, after pulsing was present.

The test of photomultiplier tubes and photodiodes at Harvard Cyclotron Laboratory measured the output current as a function of incident proton flux. The resonse was slightly less than linear for most of the devices tested. The radiation resistance of each device was calculated by comparing the radiation response to the peak response to an incident optical flux. The photomultipliers were more radiation resistant than the other devices tested. Among the photodiodes the avalanche photodiodes were the most resistent to transient effects.

Some long term or permanent effects were observed during this test. These would affect an electro-optical system even after the particle beam was turned off. In the photomultipliers measurable residual currents were observed for minutes after the beam was turned off. This was probably caused by phosphorescence. Two decay constants were observed. The long term effects in the photodiodes lasted for at least hours at room temperature. They were probably caused by displacement damage increasing the density of recombination centers and increasing the leakage current.

Finally the results of these measurements were used to determine the effects of protons on performance of two systems. One system was an imaging system of moderate resolution which uses photodiodes for use in geosynchronous orbit. The signal-to-noise was 60 for the system. This was reduced below 5.5 (the lowest desired level) for radiation induced currents in excess of 1×10^{-7}A.

The second system considered was a tracking system using an image dissector camera. First the radiation current to produce a signal-to-noise of 5.5 for a given object was calculated. Then the acquisition time for various radiation currents and objects was determined and finally the signal-to-noise was calculated.

Future work in this area is desirable to extend these measurements to new operating conditions, new devices and materials, other physical effects, more extensive modeling, and different particles. These sensors and others can be tested in various operating modes such as differing bias conditions, operating with a light source, pulse counting, etc. More detailed models can be developed to explain and predict radiation effects. Effects such as funneling and nuclear reactions which are present only for energetic heavy ions can be measured. Many other devices not as familiar for space flight applications are currently being developed or are on the market. These should be tested.

REFERENCES

1. H.R. Zwicke, Photoemissive Detectors, in Topics in Applied Physics: Optical and Infrared Detectors, ed R.J. Keyes, Springe-Verlag, 1977.

2. C.E. Barns & J.J. Wiczer, Radiation Effects in Optoelectronic Devices, Sandia National Laboratories, DE84 012889, 1984.

3. G.E. Stillman and C.M. Wolfe, Avalanche Photodiodes, in Semiconductors and Semimetals Vol 12: Infrared Detectors II, ed R.K. Willardson and A.C. Beer, Acadamic Press, N.Y., 1977.

4. Stephen F. Jacobs, Nonimaging Detectors, in Handbook of Optics, ed W.G. Driscoll and W. Vaughn, McGraw-Hill Book Company, 1978.

5. R.D. Hudson, Infrared System Engineering, John Wiley and Sons, New York, 1969.

6. L.K. Anderson and B.J. McMurtry, High-Speed Photodetectors, Proc. IEEE Vol. 54, 1966.

7. Silicon Photodetector Design Manual, United Detector Technology, Inc.

8. R.W. Engstrom, RCA Photomultiplier Handbook, RCA Solid-State Division, 1962.

9. S.M. Sze, Physics of Semiconductor Devices, John Wiley and Sons, Inc., 1981.

10. J.L. Wirth and S.C. Rogers, IEEE Transactions on Nuclear Science, 11, 24, Nov. 1964.

11. F.B. McLean and T.R. Oldham, Charge Funneling in N- and P-type SI Substrates, IEEE Transactions on Nuclear Science, NS29, 1982.

12. G.C. Messenger, Collection of Charge on Junction Nodes from Ion Tracks, IEEE Transactions on Nuclear Science, NS29, 1982.

13. E.L. Peterson, Single Event Upsets in Space, AIAA 21st Aerospace Sciences Meeting, 1983.

14. P.J. McNulty and G.E. Farrell, Proton-Induced Nuclear Reactions in Silicon, IEEE Transactions on Nuclear Science, NS-28, 1981.

15. P.J. McNulty, G.E. Farrell, R.C. Wyatt, P.L. Rothwell, and R.C. Filz, Upset Phenomena Induced by Energetic Protons and Electrons, IEEE Transactions on Nuclear Science, NS-27, 1980.

16. E. Peterson, Soft Errors Due to Protons in the Radiation Belt, IEEE Transactions on Nuclear Science, NS-28, 1981.

17. W.E. Price, D.K. Nichols, and K.A. Soliman, A Study of Single Event Upsets in Static RAM's, IEEE Transactions on Nuclear Science, NS-27, 1980.

18. W. Budde, Optical Radiation Measurements, in Physical Detectors of Optical Radiation, Vol 4, Ed F. Grum and C. Bartleson, Academic Press, 1983.

19. H.S. Zagirites and D.Y. Lee, Gamma and X-Ray Effects in Multiplier Phototubes, IEEE Transactions on Nuclear Science, NS-12, 1965.

20. A.J. Favale, F.J. Kuehne, and M.D. D'Agostino, Electron Induced Noise in Star Tracker Photomultiplier Tubes, IEEE Transactions on Nuclear Science, NS-14, 1967.

21. M. Johnson, Radiation Effects on Multiplier Phototubes, IEEE Transaction on Nuclear Science, NS-20, 1973.

22. W. Viehmann and A.G. Eubanks, Noise Limitations of Multiplier Phototubes in the Radiation Environment of Space, NASA Technical Note NASA TN D-8147, 1976.

23. L.W. Howell and H.F. Kennel, A Stochastic Model for Photon Noise Induced by Charged Particles in Multiplier Phototubes of the Space Telescope Fine Guidance Sensors, NASA Technical Paper 2337, 1984.

24. W. Viehmann, A.G. Eubanks, G.F. Pieper, and J.H. Bredekamp, Photomultiplier Window Materials Under Electron I Radiation: Fluorescence and Phosphorescence, Applied Optics, Vol 14, 1975.

25. S.M. Johnson, Radiation Effects on Multiplier Phototubes, IEEE Transactions on Nuclear Science, NS-20, 1973.

26. A.H. Kalma and W.H. Hardwick, Radiation Testing of PIN Photodiodes, IEEE Transactions on Nuclear Science, NS-25, 1978.

27. W.H. Hardwick and A.H. Kalma, Effects of Low-Dose-Rate Radiation on Opto-Electronic Components and the Consequences Upon Fiber Optic Data Link Performance, IEEE Transactions on Nuclear Science, NS-26, 1979.

28. J.J. Wiczer, L.R. Dawson, and C.E. Barnes, Transient Effects of Ionizing Radiation in Photodiodes, IEEE Transactions, NS-28, 1981.

29. E.H. Eberhardt, The Image Dissector as an Optical Tracker, Paper Presented at the Optical Tracking Seminar of the Society of Photo-Optical Instrumentation Engineers, 1971.

END

FILMED

1-86

DTIC